Molecular Cell

Article

Nucleosomes specify co-factor access to p53

Graphical abstract

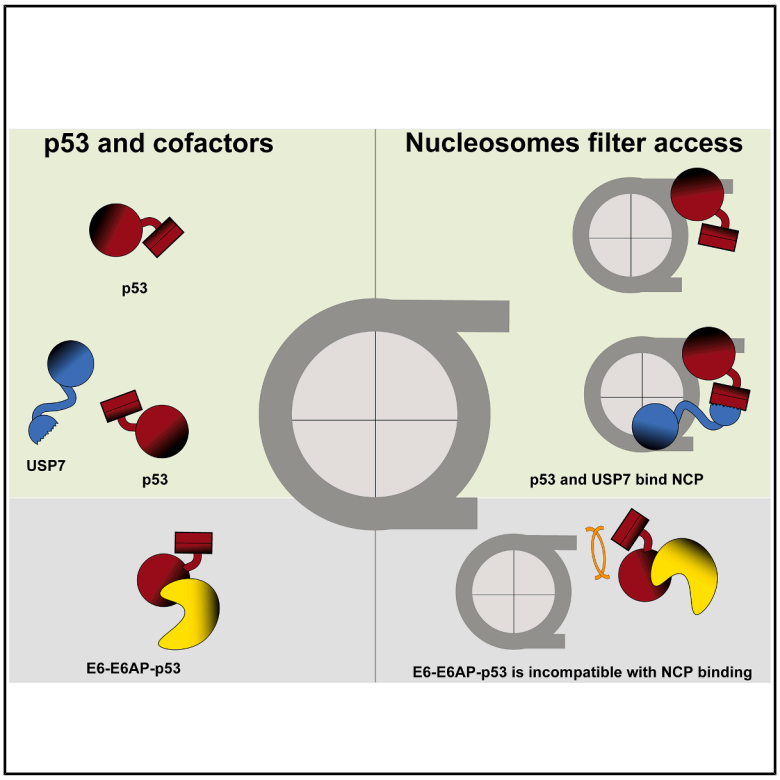

Highlights

- Cryo-EM studies show p53-histone binding via DBD/TET at distinct nucleosome sites
- Biochemical and cryo-EM studies reveal full-length USP7-p53-nucleosome complex
- Deubiquitinating enzyme USP7 is active in the vicinity of chromatin-bound p53
- Cryo-EM shows that monomeric and dimeric E6AP-E6-p53 complex cannot bind nucleosome

Authors

Deyasini Chakraborty, Colby R. Sandate, Luke Isbel, ..., Dirk Schübeler, Alicia K. Michael, Nicolas H. Thomä

Correspondence

nicolas.thoma@epfl.ch

In brief

Chakraborty, Sandate, et al. report that chromatin-bound p53 interacts with deubiquitinating enzyme USP7 but not with the E3 ubiquitin ligase E6AP-E6, despite both co-factors being associated with the ubiquitin proteasome system that regulates p53 levels. This study highlights the critical role of chromatin in determining the interaction of p53 with its regulatory co-factors.

Chakraborty et al., 2025, Molecular Cell *85*, 2919–2936
August 7, 2025
https://doi.org/10.1016/j.molcel.2025.06.027

CellPress

Molecular Cell

CellPress
OPEN ACCESS

Article

Nucleosomes specify co-factor access to p53

Deyasini Chakraborty,[1,2,10] Colby R. Sandate,[1,3,10] Luke Isbel,[1,4,5] Georg Kempf,[1] Joscha Weiss,[1,2] Simone Cavadini,[1] Lukas Kater,[1] Jan Seebacher,[1] Zuzanna Kozicka,[1,6,7] Lisa Stoos,[1,2] Ralph S. Grand,[1,8] Dirk Schübeler,[1,2] Alicia K. Michael,[1,9] and Nicolas H. Thomä[1,3,11,*]

[1]Friedrich Miescher Institute for Biomedical Research, Basel, Switzerland
[2]University of Basel, Basel, Switzerland
[3]School of Life Sciences, Ecole Polytechnique Fédérale de Lausanne (EPFL), Lausanne, Switzerland
[4]Present address: The University of Adelaide, South Australian immunoGENomics Cancer Institute, Adelaide, SA, Australia
[5]Present address: Adelaide Centre for Epigenetics, Faculty of Health and Medical Sciences, The University of Adelaide, Adelaide, SA, Australia
[6]Present address: Department of Medical Oncology, Dana-Farber Cancer Institute, Boston, MA, USA
[7]Present address: Broad Institute of MIT and Harvard, Cambridge, MA, USA
[8]Present address: Zentrum für Molekulare Biologie der Universität Heidelberg, Heidelberg, Germany
[9]Present address: Institute of Science and Technology Austria, Klosterneuburg, Austria
[10]These authors contributed equally
[11]Lead contact
*Correspondence: nicolas.thoma@epfl.ch
https://doi.org/10.1016/j.molcel.2025.06.027

SUMMARY

Pioneer transcription factors (TFs) engage chromatinized DNA motifs. However, it is unclear how the resultant TF-nucleosome complexes are decoded by co-factors. In humans, the TF p53 regulates cell-cycle progression, apoptosis, and the DNA damage response, with a large fraction of p53-bound sites residing in nucleosome-harboring inaccessible chromatin. We examined the interaction of chromatin-bound p53 with co-factors belonging to the ubiquitin proteasome system (UPS). At two distinct motif locations on the nucleosome (super-helical location [SHL]−5.7 and SHL+5.9), the E3 ubiquitin ligase E6-E6AP was unable to bind nucleosome-engaged p53. The deubiquitinase USP7, on the other hand, readily engages nucleosome-bound p53 *in vitro* and in cells. A corresponding cryo-electron microscopy (cryo-EM) structure shows USP7 engaged with p53 and nucleosomes. Our work illustrates how chromatin imposes a co-factor-selective barrier for p53 interactors, whereby flexibly tethered interaction domains of co-factors and TFs govern compatibility between co-factors, TFs, and chromatin.

INTRODUCTION

The repeating nucleosome units in the genome are principally viewed as repressive to most protein binding,[1–6] yet a subset of transcription factors (TFs) nonetheless binds to nucleosome-embedded binding sites. To reach their DNA motifs on a sterically crowded nucleosome, these TFs employ diverse strategies,[7] such as distortion of the nucleosomal DNA[8–10] or binding through a reduced DNA-binding footprint.[9] In all the structures to date, TF binding triggers intricate interactions between the nucleosome and the DNA-binding domain (DBD),[7] raising the question if and how nucleosome-bound TFs interact with transcriptional co-factors in a chromatin environment.

The tumor suppressor p53 regulates cell-cycle progression, apoptosis, and DNA repair. p53 plays an important role in safeguarding genome stability,[11–14] and it is mutated in ~50% of human cancers.[13] Genome-wide binding profiles (chromatin immunoprecipitation sequencing [ChIP-seq]) and chromatin accessibility measurements (assay for transposase-accessible chromatin with sequencing [ATAC-seq]) revealed the atypical ability of p53 to stably access a significant portion of its binding sites residing in closed chromatin prior to cellular stress.[12,15–17] While the exact nucleosomal engagement sites and binding modes are unclear, structural studies found p53 immediately juxtaposed to nucleosomes and engaging in interactions between the p53 DBD and the histone H3 tail.[18] The diverse cellular roles of p53 require a large network of co-factors and regulators,[14] rendering p53 an excellent model system for studying the TF interplay among nucleosomes and diverse co-factors.

Cellular p53 levels are controlled by the ubiquitin proteasome system (UPS).[19,20] To examine how chromatin impacts the accessibility of p53 to the members of the UPS, we chose two p53-specific multi-domain enzymes: the E3 ubiquitin ligase E6AP[19] and the deubiquitinase (DUB) USP7 (also known as HAUSP).[21] Each specifically targets p53 and in parallel also acts as global regulators of protein homeostasis through other additional substrates.

Multiple E3 ubiquitin ligases, including E6AP and MDM2, directly control p53 levels.[19,20,22,23] p53 is involved in a negative

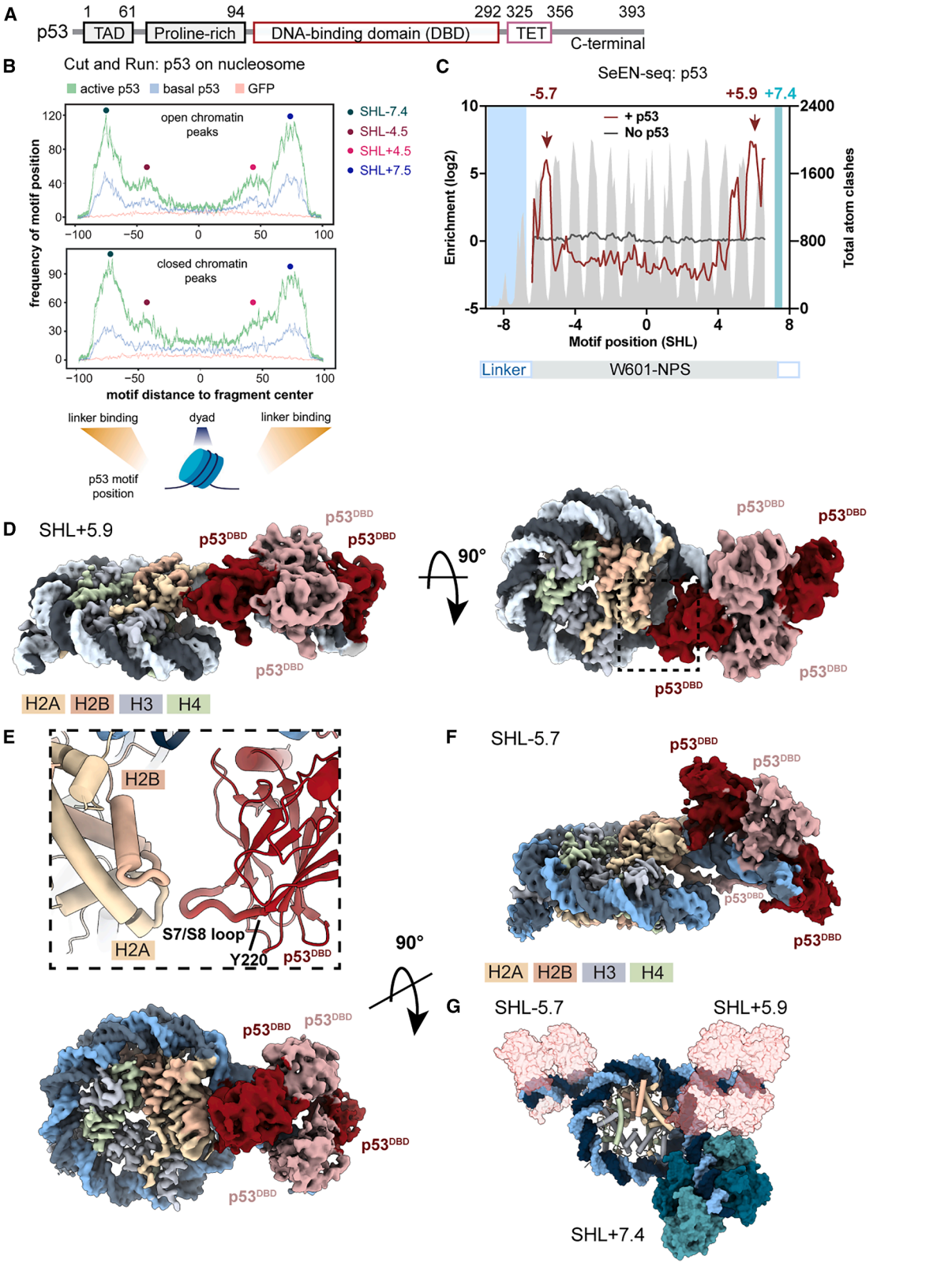

(legend on next page)

feedback loop with MDM2, where it is continuously ubiquitinated and turned over to maintain steady-state levels in cells.[24,25] Upon cellular stress and the ensuing checkpoint kinase response, MDM2/MDMX become phosphorylated and lose affinity to p53. p53 then switches binding partners to the DUB USP7, leading to increased p53 levels.[26,27] Decreased levels of USP7, on the other hand, stabilize p53 as USP7 also deubiquitinates and thereby stabilizes MDM2 and MDMX[28–31] under stress-free conditions. Taken together, USP7 activity is an important regulator of p53 function. USP7 is a multi-domain enzyme consisting of an N-terminal substrate-binding tumor necrosis factor (TNF) receptor-associated factor (TRAF) domain, a catalytic domain (CD), and five C-terminal ubiquitin-like (UBL) domains.[32] Structural studies have shown that the N-terminal TRAF domain engages the p53 tetramerization (TET) domain.[33] Beyond p53, many of the known USP7 targets are nuclear proteins[34]: USP7 acts as a DUB for the TF HIF-1α, regulating ordered recruitment of CBP, and the CDK8-Mediator assemblies as well as transcriptional elongation complexes.[35] Additional nuclear substrates include TFs like FOXO4[36] and MGA,[37] histones H3 and H2B,[38,39] members of the DNA replication (DNMT1, Geminin,[40,41] and MCM-BP[40,41]) and DNA repair machinery (XPC[42,43] and UVSSA[42,43]), and the histone demethyltransferase PHF.[44]

Several viral proteins also target p53.[45] Best characterized are the malignant variants of the human papilloma virus (HPV). The HPV protein E6 serves as a p53 adaptor and triggers degradation by recruiting the homologous to the E6AP carboxyl terminus (HECT) E3 ligase E6-associated protein (E6AP, also known as UBE3A),[19] but whether E6-E6AP impacts p53 function in a non-enzymatic fashion is unclear. The multi-subunit E6AP contains several domains, including an amino-terminal zinc-binding domain (AZUL),[46] an LxxLL motif implicated in binding nuclear hormone receptors,[47] and the catalytic HECT domain. Besides its pathogenic role in p53 degradation, E6AP ubiquitinates several substrates including PML,[48] annexin A1,[49] MAPK1, CDK1, CDK4, and β-catenin.[50] E6AP loss-of-function mutations lead to Angelman syndrome and Angelman syndrome-like symptoms, while the E6AP gene duplication is associated with autism spectrum disorder.[51–53]

Using a p53-specific E3 and DUB co-factor pair, we mapped the spatial restrictions for engaging p53 bound to physiological sites on nucleosomes. Through biophysical methods and cryoelectron microscopy (cryo-EM), we found that the DUB USP7 accesses p53 while it is engaged on the nucleosome; the multimeric E6-E6AP-bound p53 in the viral ternary complex, on the other hand, sterically prevents p53 from binding chromatin. The manner where and how these co-factors engage p53 determine whether the p53/co-factor complex is compatible with or mutually exclusive to nucleosome binding. This work reveals a set of simple spatial rules for how flexibly tethered interaction domains as part of the co-factor and TF enable cohabitation in the spatially crowded environment of TF-nucleosome complexes.

RESULTS

p53 preferentially binds nucleosomes near entry/exit sites and linkers

To identify physiological substrates for p53 and co-factors on chromatin, we investigated the binding behavior of p53 in cells as well as the detailed nucleosomal registers engaged by p53 *in vitro*. Levels of p53 are rapidly induced in response to various cellular stresses.[54] Genome-wide measurement of chromatin accessibility in mouse stem cells, using ATAC-seq, revealed that p53 situated in closed chromatin.[12,15–17] p53 sites in closed chromatin become more accessible following activation of the DNA damage stress response.[15] To define the chromatin binding preferences of p53 in the presence and absence of cellular stress, we carried out CUT&RUN (C&R), through targeting a nucleosome-sensitive micrococcal nuclease to p53-binding sites and analyzing the digestion pattern (Figures 1B and S1A–S1D).[55,56] The genomic DNA digestion pattern is impacted by the presence of nucleosomes with their characteristic footprint of ∼145 to 147 base pairs (bp) DNA wrapped around an octamer of histones including H4, H3, H2A, and H2B.[6] We found that C&R enrichment scaled with the ChIP-seq signals for both basal and "activated" p53 under cellular stress conditions (Figure 1B). The overall p53-binding nucleosome-engagement profile was similar at open and closed chromatin. The corresponding V-plot analysis found micrococcal digestion fragments in the range of ∼157–237 nucleotides (nt), best explained by p53 motifs protected from digestion through a nearby nucleosome (Figure S1E). While some fragments are not indicative of nucleosomes (i.e., larger or sub-nucleosomal sized), the majority of signal are consistent with p53 binding at multiple positions along the nucleosomal DNA trajectory with strong positioning of binding sites ranging from the inter-nucleosomal linker to the nucleosomal DNA entry/exit site (Figures 1B and S1F–S1H).

The canonical p53 motif encompasses two CATG units separated by a 6-bp linker, where p53 binding is mediated by its four

Figure 1. p53 binds at multiple motif registers on the nucleosome

(A) Domain schematic of transcription factor (TF) p53. TAD, transactivation domain; DBD, DNA-binding domain; TET, tetramerization domain. The full-length construct (human p53 residues 1–393) has been used in the study.

(B) CUT&RUN profile showing the binding of p53 relative to the nucleosome.

(C) SeEN-seq profile of p53 showing end-binding preference on the nucleosome (NCP) using a W601 sequence. The p53 motif used in this study is AACATGCCCGGGCATGTC, and the motif position is indicated by SHLs that describe where the major groove of nucleosomal DNA faces the histones. The SHLs have been determined following the centroid of the motif. The nucleosomes (100 nM) were incubated with p53 (250 nM) for the assay. The enrichment values are shown as average of independent replicates (n = 3). Computationally predicted atomic clash of the TF with NCP is overlaid (gray). The blue region indicates the linker nucleosomal DNA.

(D) Cryo-EM maps of p53 bound to its motif at SHL+5.9. $p53^{DBD}$ are shown in light and dark red, DNA as pale blue and gray, and histones are colored as indicated.

(E) Potential histone interaction between the S7/S8 loop of p53 and H2A and H2B.

(F) Cryo-EM map of p53 bound to its motif at SHL−5.7. Density is colored as in (E); however, DNA is shown in light and dark gray.

(G) Superposition of p53-$NCP^{SHL+5.9}$, p53-$NCP^{SHL-5.7}$, and p53-$NCP^{SHL+7.4}$ structure from Nishimura et al.,[18] aligned on the nucleosome. $p53^{DBD}$ structures at SHL−5.7 and SHL+5.9 are shown in red and semi-transparent, while the linker DNA structure at SHL+7.4 is shown in green.

DBDs ($p53^{DBD}$), with each CATG bound by two $p53^{DBD}$ monomers.[54] DBD oligomerization is facilitated by a TET domain ($p53^{TET}$, also known as the oligomerization domain) connected to the $p53^{DBD}$ at its C terminus through a flexible linker[57,58] (Figure 1A). We refer to TF-binding sites on nucleosomes in terms of "super-helical locations" (SHLs) defined by the sites on nucleosomal DNA. The dyad is denoted as SHL0, and DNA helical turns emanating from the dyad to the entry/exit sites are progressively numbered as SHL±1–7. Previous biochemical studies tested three selected p53 motifs locations at the ends of the nucleosome DNA (SHL±6.5, SHL±7.0, SHL±8.0) as well as tiling different promoter sequences across parts of the nucleosome.[18,59–61]

To precisely map p53 binding at base-paired resolution throughout the entire nucleosome and the linker, we used selected engagement on nucleosome sequencing (SeEN-seq).[9] In SeEN-seq, a library of p53 DNA substrates is generated by tiling a high-affinity p53 motif (AACATGCCCGGGCATGTC[62]) throughout every possible position of a Widom 601 nucleosome positioning sequence[63] throughout the nucleosome between SHL−6.4 and SHL+6.5. Upon addition of recombinant p53 to nucleosomes reconstituted with this DNA library, binding is measured *in vitro* through a combination of electromobility shift assays (EMSAs) and next-generation sequencing (NGS) methodology (Figure 1C). The SeEN-seq profiles found p53 with preferred binding at SHL−5.7 and SHL+5.9 (Figure 1C), identifying an overall p53-binding preference at the entry/exit sites of the nucleosomal DNA (also referred to as end-binding activity) but also local minima/maxima. In SeEN-seq, p53 accessibility maxima were around SHL+5.1 to SHL+4.8, and accessibility peaks decreased in amplitude as the motif was positioned closer to the dyad (Figure 1C). Calculating expected clash scores using a canonical nucleosome as template (Figure 1C), we not only found that the observed SeEN-seq accessibility peaks increased with distance to the nucleosomal dyad, but we also found a ~10-bp periodicity in peak regions. These highly accessible regions coincided with solvent-exposed, and hence intrinsically more accessible, motif positions on nucleosomes (in agreement with Wilson et al.,[61] where diverse motifs were tested for p53, p63, and p73).

We then wanted to quantify binding at a preferred nucleosome-internal position $NCP^{SHL-5.7}$ versus more distal sites including $NCP^{SHL-7.4}$ (see also Nishimura et al.[18]) and $NCP^{SHL-7.7}$. EMSA experiments showed similar apparent affinities on the order of ~300–350 nM for the three NCP substrates (Figures S2B–S2E). The distal sites at SHL−7.7 and SHL−7.4 showed slightly tighter binding ($NCP^{SHL-7.4}$: ~300 nM; $NCP^{SHL-7.7}$: ~310 nM), compared with the internal motif ~335 nM $NCP^{SHL-5.7}$. A trend for slightly tighter binding at distal positions was also evident in an SeEN-seq experiment where a 20-bp linker attached to a Widom 601 sequence was tiled at base-paired resolution (Figure S2A). We conclude that overall, p53 binds nucleosomal motifs at the entry/exit site with surprising ease, with a slight preference in engaging more distal sites toward the linker.

p53 interacts with histones through its DBD and TET domains

Next, we set out to elucidate the binding mechanism of p53 at nucleosome-internal sites. Based on the enrichment peaks obtained with SeEN-seq, we chose SHL+5.9 and SHL−5.7 for in-depth analysis (Figure 1C). At the site 59 bp away from the nucleosomal dyad (SHL+5.9), we were able to determine a cryo-EM structure of nucleosome-bound p53 at an overall resolution of 3.8 Å ($p53\text{-}NCP^{SHL+5.9}$) (Figure 1D; see Figure S3 for local resolution plots) as well as a second cryo-EM structure, located 57 bp away from the dyad in a different nucleosomal register at SHL−5.7 ($p53\text{-}NCP^{SHL-5.7}$) at 3.3 Å (Figure 1F; see Figure S4 for local resolution plots). In $p53\text{-}NCP^{SHL+5.9}$ and $p53\text{-}NCP^{SHL-5.7}$, p53 binds as a tetramer with its four well-resolved DBDs engaged to a full DNA motif. To gain access to the 18-bp motif, p53 stabilizes the unwrapped nucleosomal DNA at the entry and exit sites around histone H2B; DNA is removed from ~SHL+4.3 to SHL+7.3 and from ~SHL−4.2 to SHL−7.3 in the $p53\text{-}NCP^{SHL+5.9}$ and $p53\text{-}NCP^{SHL-5.7}$ structures, respectively. The positions of the p53 motif at SHL−5.7 and SHL+5.9 are nearly pseudo-symmetric with respect to the dyad axis of the nucleosome (Figure 1G), yet the slight change in motif positioning gives rise to different DNA trajectories with very distinct p53-histone interactions. The more internal complex at SHL−5.7 shows a lower angle of DNA deflection (~50°), relative to a canonical nucleosomal DNA template, than the slightly more distal complex at SHL+5.9 (~120°) (Figure S5A). In the $p53\text{-}NCP^{SHL+5.9}$ structure, the p53 S7/S8 loop (residues 220–228) on the $p53^{DBD}$ is proximal to H2A (residues 75–80) and H2B (residues 48–56) (Figure 1E), while no such histone contacts were observed in the $p53\text{-}NCP^{SHL-5.7}$ structure (Figure 1F). We note that residue 220 of $p53^{DBD}$, which is frequently mutated (Y220C) in various cancers and can serve as a binding site for small molecules,[64–66] is oriented toward the histone interface. Previous nucleosomal interactions observed for p53 located at the linker-proximal site (SHL+7.4, Figure 1G)[18] displayed less unwrapping to accommodate p53 on a 21-bp DNA motif. In this case, the $p53^{DBD}$ helix 1 (H1, residues 166–168) approached the N-terminal tail of H3 (residues 38–40) (Figure S5D).

In addition to resolving non-crosslinked structures of p53 at two different nucleosomal registers, we performed gradient fixation (GraFix)[67,68] crosslinking to determine cryo-EM structures of $p53\text{-}NCP^{SHL-5.7}$ and $p53\text{-}NCP^{SHL+5.9}$ at similar SHLs selected for the non-crosslinked complexes (Figures 2A and S5F for the $p53\text{-}NCP^{SHL+5.9}$ complex). The crosslinked $p53\text{-}NCP^{SHL-5.7}$ complex revealed an additional density in the proximity of the histone core (Figure 2A). The only structured part absent from our previous model was the more flexible $p53^{TET}$ domain. Crosslinking mass spectrometry (XL-MS) studies of $p53\text{-}NCP^{SHL-5.7}$ revealed intermolecular crosslinks between p53 and histones H2A (K357:K75) and H3 (K357:K57), and the additional density was assigned accordingly as the $p53^{TET}$ based on density, crosslink, and energy-guided docking simulations (Figures 2B, S2E, S5E, S6G, and S6H). Comparing SHL+5.9 and SHL−5.7 structures, the interactions between the $p53^{DBD}$ and $p53^{TET}$ at SHL−5.7 are accommodated through a rotation of the DBD tetramer relative to the nucleosome, thereby forgoing the DBD/histone contacts observed in the SHL+5.9 structure. During the cryo-EM image processing (Figures S7 and S8), classifying out a well-defined DNA trajectory for the $p53^{DBD}$, we tended to lose the highly flexible $p53^{TET}$ domain density gradually, even in the crosslinked sample. This suggests the existence of multiple, flexible interaction modes among the $p53^{TET}$, the $p53^{DBD}$,

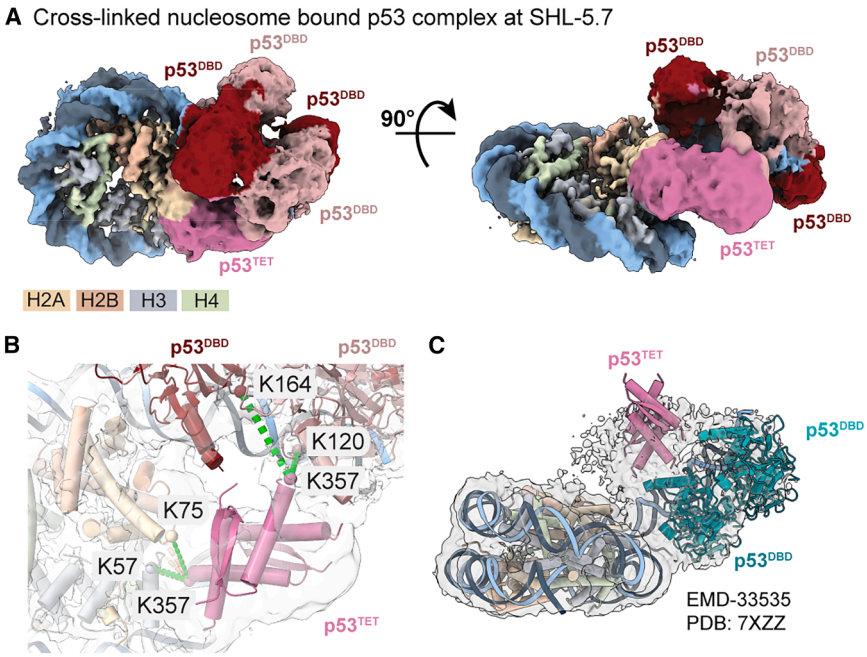

Figure 2. p53 binds at multiple motif registers on the nucleosome

(A) Cryo-EM map of GraFix stabilized samples of p53 bound to nucleosome at SHL−5.7 wherein there is an indication of an extra density, compared with the non-crosslinked maps shown in Figure 1F.

(B) Crosslinking mass spectrometry studies indicate crosslinks between $p53^{TET}$ and $p53^{DBD}$, also crosslinks between $p53^{TET}$ and the histones. Model for $p53^{TET}$ domain is derived from density, crosslink, and energy-guided docking simulations.

(C) Superposition of $p53^{DBD}$ tetramer and $p53^{TET}$ (pink) from the p53-$NCP^{SHL+5.9}$ structure with the $p53^{DBD}$ tetramer from a previously published p53-$NCP^{SHL+7.4}$ structure[18] (green), suggesting that previously non-assigned cryo-EM density corresponds to the $p53^{TET}$ domain.

and the nucleosome. Interestingly, unassigned density near the $p53^{DBD}$ tetramer was also observed in the previous structure of p53 bound at SHL+7.4.[18] Aligning our p53 model to this structure revealed co-localization of the $p53^{TET}$ within this density (Figure 2C). The $p53^{TET}$ has previously been reported to enhance the binding capacity of p53 *in vitro* and in cells.[57] This domain placed into p53-nucleosome structures at SHL−5.7 and SHL+5.9 is ideally positioned to prevent re-wrapping of the nucleosomal DNA, potentially facilitating p53 access to the motif. Consistent with this, a recent structure of TF NR5A2 binding to nucleosome exhibits a somewhat related strategy to prevent DNA re-wrapping involving its C-terminal extension (CTE) loop.[60]

Overall, the three p53-NCP structures effectively illustrate how different motif registers give rise to differential nucleosome interactions involving the $p53^{DBD}$ as well as distal domains such as $p53^{TET}$. These structures are governed by three different motif registers with different interactomes and give rise to structurally distinct p53/nucleosome substrates to be read out by co-factors that recognize both p53 and the nucleosome.

p53 nucleosome binding differentially impacts co-factor binding

We next tested co-factor binding to p53 at *in vitro* and *in vivo* high-affinity/high-occupancy sites at SHL+5.9 and SHL−5.7, using the co-factors USP7 or E6-E6AP.

In analytical size-exclusion chromatography (SEC), full-length USP7 or E6-E6AP were injected together with p53 and reconstituted nucleosomes containing a p53 motif at SHL−5.7 or SHL+5.9 ($NCP^{SHL-5.7}$ and $NCP^{SHL+5.9}$) (Figures 3B and 3C). The UV absorbance at a wavelength of 254 nm indicated absorption by nucleic acids while that of 280 nm was indicative of absorption by proteins. At both motif locations, the USP7 elution profile showed clear comigration with p53 and histones (Figures 3B and 3C, panel 1), with a similar behavior observed in the SEC-MALS (Figure S16B; extended Table 1). USP7 without p53 showed no detectable shift or comigration with nucleosomes ($NCP^{SHL-5.7}$) (Figure S9F). This suggests that high-affinity USP7 recruitment to nucleosomes depends on p53 (Figures 3B and 3C, panel 1). In contrast, the elution profile of E6-E6AP with p53 and nucleosomes ($NCP^{SHL-5.7}$ or $NCP^{SHL+5.9}$) did not show comigration with the histone core (Figures 3B and 3C, panel 2). Similarly, in mass photometry (MP), the E6AP-E6-p53 ternary complex measured in the presence and absence of $NCP^{SHL-5.7}$ had nearly identical mass profiles, differing only with a peak around ~190 kDa, which corresponded to uncomplexed $NCP^{SHL-5.7}$ (Figures S10A and S10B). Fluorescence polarization measurements with a fluorescent oligo indicated that the E6AP-E6-p53 complex could nonetheless bind to nucleic acids and exhibited some level of preferential binding to p53 motifs over a scrambled wild-type control (Figures S10C–S10E). Flow-induced dispersion analysis (FIDA) of E6AP-E6-p53 with fluorescently labeled free DNA (Figure S10F) or NCP (Figure S10G) likewise showed an attenuated affinity for DNA but not nucleosomes. Additionally, in our SEC experiments, we used a fluorescein (FAM)-labeled p53 motif as the oligo to test its binding with the E6AP-E6-p53 complex and observed a peak with an emission signal at 516 nm coeluting with the E6AP-E6-p53 complex (Figures S10H and S10I). Together, these data indicate that USP7 has high affinity for nucleosome-bound p53 at SHL−5.7 and SHL+5.9 (Figures 3B and 3C), while binding of E6AP-E6-p53 to these two nucleosomal substrates was not detectable.

The E6-E6AP architecture is incompatible with nucleosome binding

To dissect the structural basis for the incompatibility between E6-E6AP-engaged p53 and nucleosomes and to preserve the native oligomeric state of p53 while in complex with E6-E6AP, we subjected the E6AP-E6-p53 complex to single particle cryo-EM analysis using full-length constructs. Purified proteins were subjected to GraFix[67] using bissulfosuccinimidyl suberate

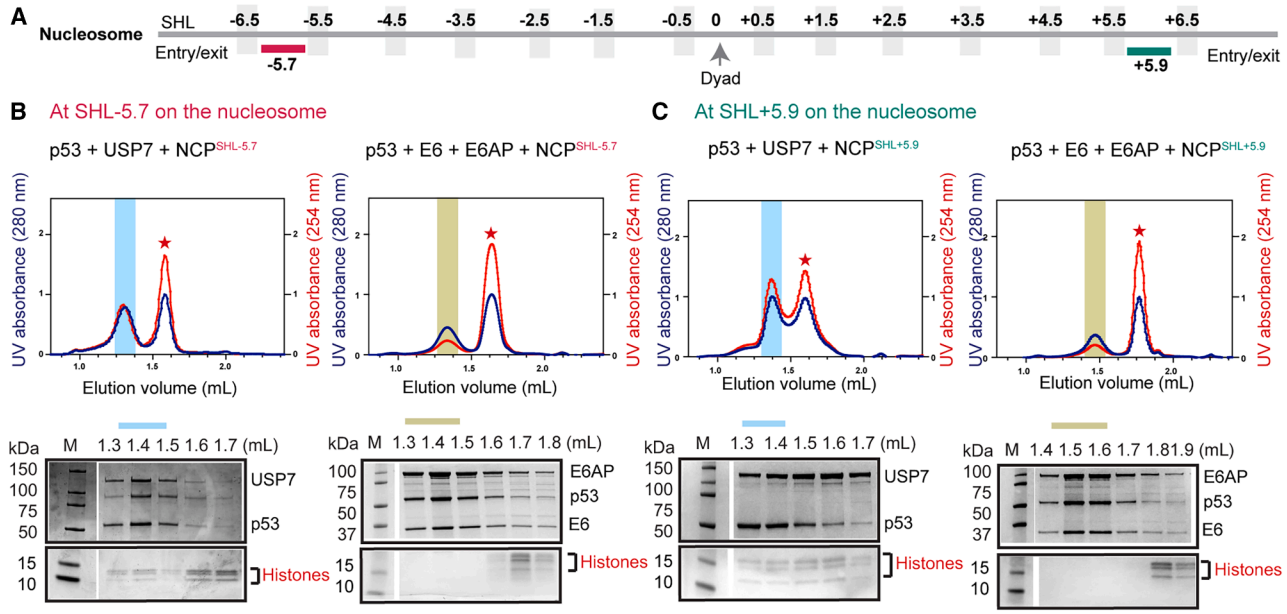

Figure 3. p53 forms complex with subset of its interactors on the chromatin

(A) The two sites on the nucleosome (SHL−5.7 labeled in red, and SHL+5.9 labeled in green) have been selected from the SeEN-seq assay in Figure 1C.

(B) Size-exclusion chromatography (SEC) profiles of p53, USP7, and E6-E6AP with nucleosome containing p53 motif at SHL−5.7 are shown on the upper panel. The UV absorbance at a wavelength of 254 nm indicates absorption by nucleic acids while that of 280 nm is indicative of absorption by proteins. The blue region in panel 1 indicates comigration of p53 and USP7 with histones. The SDS-PAGE profiles show elution of the respective proteins. The light green region in panel 2 indicates the formation of ternary complex of p53 with E6-E6AP but does not indicate comigration with histones, as also indicated in the SDS-PAGE in the lower panel.

(C) At the second entry/exit site, SHL+5.9 (in green) on the nucleosome, SEC profiles show comigration of histones with p53 and USP7 (labeled in blue, panel 1), whereas the ternary complex of p53 with E6-E6AP (labeled in light green, panel 2) do not show association with histones.

(BS3) (Figure 4A) or glutaraldehyde (GA) crosslinking (Figure 4B), yielding structures at 3.7 and 4 Å, respectively (Figures S11 and S12).

The BS3-crosslinked structure was in line with published X-ray structures of truncated p53, E6, E6AP,[69] and a recently published cryo-EM study of a ternary complex formed between $p53^{DBD}$ and full-length E6AP-E6.[70] Our structure includes a single copy of E6AP, E6, and $p53^{DBD}$, with the HECT domain of E6AP visible in the characteristic L-conformation and where its LxxLL motif is sandwiched between the two zinc-binding domains of E6 (Figure 4A). A large helical domain in E6AP (130–516), previously unresolved in X-ray structures but now annotated by our structure and others,[70,71] forms an extended interface outside of the LxxLL motif with p53 (Figure 4A) and E6, which we designate the E6-p53-interacting (EPI) domain.

In the presence of the GA crosslinker, we observed a C_2-symmetric envelope consistent with a dimer of ternary complexes with two copies each of E6AP, E6, and $p53^{DBD}$ (Figure 4B). Reprocessing the BS3 dataset with increased ice thickness to preserve larger assemblies combined with reference-free two-dimensional (2D) classification and three-dimensional (3D) reconstruction revealed a similar dimeric ternary complex (Figure S11). The reconciled previous in-solution MP results with non-crosslinked samples depict peaks that agree with calculated molecular weights of ternary complexes with 2:2:2, 3:3:3, and 4:4:4 stoichiometry (Figure S10A). MP measurement with ternary complexes composed of truncated p53 that only contains the DBD, on the other hand, depicts peaks with smaller complexes with a calculated stoichiometry of 2:2:2 (Figure S10B). Together, these data suggest that the structured core of the ternary complex is in an equilibrium between monomeric (1:1:1) and dimeric (2:2:2) assembly states but can also form larger stoichiometries through further oligomerization induced by the $p53^{TET}$ domain. Although not resolved in either of our structures, the $p53^{TET}$ domain can be expected to combine the monomeric and dimeric building blocks, creating higher-order assemblies. In line with these biochemical findings, two copies of the monomeric ternary complex were hence used to fit within the C_2-symmetric density. This was possible without any notable structural changes. The main interface (740 $Å^2$) between the two dimers comprises the E6AP N-terminal α helices (Figure S13A), with a smaller (160 $Å^2$) interface formed by the two copies of $p53^{DBD}$, each bound to one copy of E6 and E6AP (Figure 4C), resembling the shape of a closed ring (Figure 4B). A recent study[71] determined the structure of E6-E6AP in the absence of p53 and showed that E6AP also forms a dimer when in complex with E6 (Figure S13B). This E6AP dimerization interface differed from that observed in the presence of p53 (Figure S13C).

The p53 oligomerization state, mediated either through the TET domain or by the tandem DNA motif, is important for DNA binding. In our dimeric structure, the HECT domains reside on the face of the ring that is opposite of the $p53^{DBD}$ dimer (Figure 4B). Importantly, the $p53^{DBD}$ dimer shows a ~35° rotation between p53 protomers, compared with our structures of the

Table 1. Cryo-EM data collection, refinement, and validation statistics

	p53-NCP$^{SHL-5.7}$ (+XL)	p53-NCP$^{SHL-5.7}$ (−XL)	p53-NCP$^{SHL+5.9}$ (+XL)	p53-NCP$^{SHL+5.9}$ (−XL)	p53-USP7^{FL}-NCP$^{SHL-5.7}$	p53-E6-E6AP monomeric	p53-E6-E6AP dimeric
Data collection and processing							
Detector magnification	96,000×	75,000×	120,000×	120,000×	75,000×	120,000×	120,000×
Voltage (kV)	300	300	200	200	300	200	200
Electron exposure (e^{-}/Å^2)	50	50	50	50	50	50	50
Defocus range (μm)	−0.8 to −2.0 μm	−0.8 to −2.0 μm	−0.8 to −2.0 μm	−0.8 to −2.0 μm	−0.8 to −2.0 μm	−0.8 to −2.0 μm	−0.8 to −2.0 μm
Pixel size (Å)	0.66	0.845	0.84	1.1267	0.845	0.84	0.84
Symmetry imposed	C1	C1	C1	C1	C1	C1	C2
Initial particle images (no.)	1,592,740	2,378,971	685,286	5,688,626	8,519,086	16,800,000	11,300,000
Final particle images (no.)	10,015	20,712	17,834	71,888	18,392	297,000	85,396
Map resolution (Å); FSC threshold (0.143)	4.2	3.2	4.2	3.8	3.9	3.7	4
Map resolution range (Å)	3.5–20	2.5–10	4–15	3–10	3–15	3–11	3–11
Refinement							
Initial models used (PDB codes)	6T93; 3KMD	6T93; 3KMD	6T93; 3KMD	6T93; 3KMD	6T93; 3KMD	4XR8	monomeric complex
Model resolution (Å)	4.2	3.2	4.2	3.5	3.9	3.67	3.99
Map sharpening *B* factor (Å^2)	N/A[a]	N/A[a]	N/A[a]	−30.0 (full map); −50.0 (local refinement)	N/A[a]	159.9	174.7
Model composition							
Non-hydrogen atoms	15855	15855	15460	15971	27042	8366	16732
Protein residues	1552	1552	1559	1561	2730	1025	2050
Nucleotides	284	284	262	286	248	0	0
Ligands	0	0	0	0	4	3	6
B factors (Å^2)	288.50	83.33	449.65	104.06	412.61	213.38	120.08
Protein	301.77	85.78	458.98	106.67	435.73	213.35	120.07
DNA	265.63	79.11	432.10	99.55	312.69	N/A	N/A
Ligand	N/A	N/A	N/A	N/A	N/A	279.26	157.38
RMSD							
Bond lengths (Å)	0.008	0.008	0.006	0.004	0.015	0.008	0.006
Bond angles (°)	1.339	1.190	1.107	0.825	1.572	0.979	0.921
Validation							
MolProbity score	0.78	0.82	0.62	1.08	1.22	0.69	0.91
Clashscore	0.77	1.10	0.34	1.45	2.90	0.36	1.35
Poor rotamers (%)	0.58	0.44	0.14	0.43	0.79	0.21	0.27
Ramachandran plot							
Favored (%)	97.84	98.69	98.57	96.81	97.26	97.74	97.84
Allowed (%)	2.09	1.31	1.43	3.12	2.41	2.26	2.16
Disallowed (%)	0.07	0.00	0.00	0.07	0.33	0.00	0.00
Model-to-data fit							
CCmask	0.7531	0.7374	0.8137	0.7638	0.5724	0.53	0.55
CCbox	0.7788	0.7604	0.8362	0.8619	0.7249	0.58	0.69
CCpeaks	0.6273	0.6570	0.6581	0.7429	0.4532	0.42	0.48
CCvolume	0.7515	0.7241	0.8074	0.7577	0.5713	0.54	0.54

[a]No sharpening was applied.

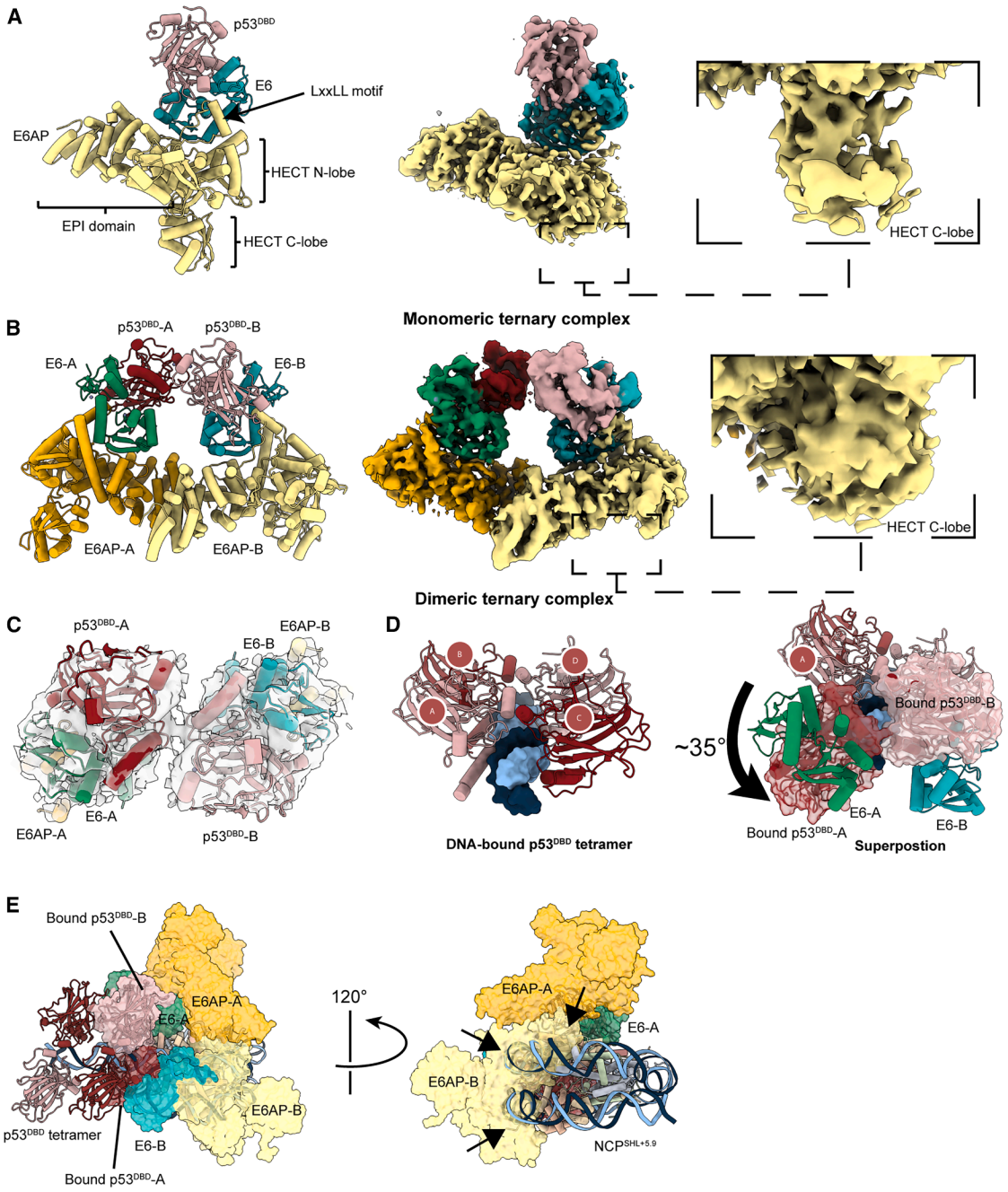

Figure 4. Cryo-EM structures of E6AP-E6-p53 ternary complex reveal multiple oligomeric states

(A) Cryo-EM structure of the monomeric ternary complex. Left: atomic model with resolved domains labeled. p53 is depicted in red, E6 in green, and E6AP in yellow. Middle: cryo-EM density map color-zoned according to atomic model at high contour value. Inset: cryo-EM density color-zoned according to atomic model at low contour value, focused on the C-lobe of the HECT domain.

(B) Cryo-EM structure of the dimeric ternary complex. Left: atomic model of the dimeric ternary complex. Both protomers of p53 are shown in red, the two E6 protomers are shown in light and dark green, and the two protomers of E6AP are depicted in yellow and dark yellow. Middle: cryo-EM density color-zoned according to atomic model at high contour value. Inset: cryo-EM density color-zoned according to atomic model at low contour value focused on the C-lobe of the HECT domain for one E6AP protomer.

(C) Zoom of the $p53^{DBD}$ dimer interface in the dimeric ternary complex. Cryo-EM density is shown as semi-transparent.

(D) The p53 dimer bound in the dimeric ternary complex is shifted from its planar orientation within the DNA-binding tetramer. Left: atomic model of $p53^{DBD}$ tetramer bound to $NCP^{SHL+5.9}$, with histones and histone-bound DNA hidden for clarity and with the four p53 protomers labeled. Right: Superposition of the p53

(legend continued on next page)

p53 tetramer on nucleosomes and crystal structures of $p53^{DBD}$ when DNA bound[72–74] (Figure 4D). Our fluorescence polarization and FIDA measurements (Figures S10C–S10G) suggest some potential p53-specific motif recognition, possibly requiring a non-canonical p53-binding mode involving only a subset of the four DBDs at a time. Accordingly, it has been previously shown that p53 dimers are able to recognize and bind p53 half-sites.[73] Yet, aligning the $p53^{DBD}$ from the E6-E6AP complex on the p53-NCP structures (SHL−5.7 or SHL+5.9) reveals severe steric clashes with the entire nucleosome architecture (Figure 4E). This suggests that E6-E6AP, when bound to the $p53^{DBD}$ directly, is structurally incompatible with nucleosomes, in line with our experimental observations (Figures 3B and 3C) and as expected given the spatial proximity between the $p53^{DBD}$ and the nucleosome at nucleosome-internal motifs (Figures 1D–1F).

USP7 and p53 form an extensive complex on chromatin

Next, we focused on the USP7-p53 complex to investigate how the multi-subunit USP7 is compatible with p53 binding in the nucleosome context. USP7 has an unstructured N terminus and a poly-Q low complexity region, followed by a TRAF domain (Figure 5A). The TRAF domain drives USP7's interaction with p53.[33] While the TRAF domain is important for substrate recognition,[33] it appears non-essential for deubiquitylation reactions involving a minimal substrate.[75] USP7's C-terminal half is divided into its CD (residues 208–560) and five UBL domains (562–1102) (Figure 5A). These UBL domains are necessary for achieving full USP7 activity.[76] X-ray structures of USP7 have resolved specific domains in isolation[34,77–79] or in association with the N-terminal TRAF (residues 54–205) and CD [77] or the C-terminal UBL domains.[80]

We used full-length USP7 for structural analysis to study the interplay of its domains with the nucleosome and p53. EMSA quantification returned a half-maximal saturation with nucleosome ($NCP^{SHL-5.7}$, Figure S15) around 3 μM. The $USP7^{FL}$-p53-$NCP^{SHL-5.7}$ complex underwent purification by density gradient centrifugation and was stabilized by GraFix crosslinking.[68] Using cryo-EM, we obtained a map of USP7 in complex with p53 bound to the nucleosome at SHL−5.7 at an overall resolution of 3.3 Å (Figures 5B and S14). The map for the p53 portion resembles our earlier structures bound at SHL−5.7, in that extensive DNA unwrapping from SHL−4.3 to −7.3 is observed on one side of the nucleosome, with clear density for the $p53^{DBD}$ tetramer. However, an additional large density extends from the region we previously attributed to the $p53^{TET}$ to hook around one side of the DNA gyre. Another additional density extends from the other side of the $p53^{TET}$ region to form a second hook across the histone face of the nucleosome. The $USP7^{FL}$-p53-$NCP^{SHL-5.7}$ map first allowed docking of a model of the tetrameric $p53^{DBD}$ wherein we observed a similar mode of nucleosomal engagement by p53 in presence and absence of USP7 (Figure S16A, see both structures superposed). However, the trajectory of the released nucleosomal DNA in the ternary complex shows slight deviation, compared with the $p53^{SHL-5.7}$ structure (Figure S16A). The local resolution of the map outside of the nucleosome and $p53^{DBD}$ tetramer was not sufficient for unambiguous placement of individual domains and required additional insight from XL-MS. The $p53^{TET}$ formed the same crosslink with histone H3 (K357:K57) as observed in p53-$NCP^{SHL-5.7}$ structure without USP7, and it presumably occupies a similar position in complex with USP7 (Figures S6 and S16C). We observed additional density between the $p53^{DBD}$ and exposed histones, corresponding to the size of a $p53^{TET}$-$USP7^{TRAF}$ heterodimer (Figures 5, S6, and S16A). This assignment was confirmed by XL-MS, yielding crosslinks between $p53^{TET}$ and histones (K351:K57 and K357:K57 from H3), as well as between $p53^{TET}$ and $USP7^{TRAF}$ (K357:K148) (Figures S6C and S16C). $USP7^{TRAF}$ and $USP7^{CD}$ are connected through a short flexible linker and were found to loosely interact in previous structures.[77] A structural unit comprising $USP7^{TRAF}$ and $USP7^{CD}$ domains is consistent with significant extra density features in the USP^{FL}-p53-$NCP^{SHL-5.7}$ structure (Figures S16A and S16C).

To resolve additional domains in the full-length USP7 structure, we used variability analysis in cryoSPARC and obtained 3D classes showing extra density with UBL domain-like features along the histone face of the nucleosome (Figure 5B). XL-MS indicates interactions between UBLs (UBL 2 and 3) and histones H2A (K96) and H3 (K57, K80, and K123) (Figures S6D and S16D). The overall structure of full-length USP7 is predicted to form a U-shaped conformation (evidence based on crosslinks, AlphaFold2 prediction, and assembled models from overlapping partial experimental structures[34]), where TRAF and CDs are on one side, UBL3–5 on the other side, and UBL1–2 acting as a hinge in the middle. This conformation is consistent with the experimentally constrained positions of $USP7^{TRAF}$ and $USP7^{UBL2-3}$ and satisfies various intra-molecular crosslinks (Figures S6 and S16E). The overall low local resolution of the map can be attributed to the flexible architecture of USP7, where UBL1–2 and UBL4–5 domains are connected through flexible linkers with UBL3, respectively. Similarly, UBL1 is connected through a rigid linker helix with the CD. In our assignment, the UBL3–5 domains reside near protein interaction "hotspots"[81] on the nucleosome, such as the acidic patch, H3 α1L1 elbow, and the H2B C helix (Figures 5D and 5E). Based on our obtained integrative model (Figure 5C; see STAR Methods), the USP7 active site is predicted to face toward the $p53^{DBD}$ tetramer. In the model, the finger-shaped β sheet (residues 369–395 and 326–347) that participates in ubiquitin binding comes close to the nucleosome-proximal $p53^{DBD}$; however, this region of USP7 is not resolved in the map. Despite the proximity to $p53^{DBD}$, $USP7^{CD}$ remains compatible with ubiquitin binding in our model (Figure S16F). The ubiquitin, in this conformation, would be sandwiched between $USP7^{CD}$ and the $p53^{DBDs}$. Lysine residues (K101, K132, K164, and K291) in the $p53^{DBD}$, which have been reported as ubiquitination sites,[82]

dimer (aligned protomer is shown in semi-transparent surface representation) and bound E6 from the dimeric ternary structure, with protomer C of the p53 tetramer bound to $NCP^{SHL+5.9}$. Arrow depicts rotation of second bound protomer relative to protomer A in the NCP-bound structure.

(E) Alignment of E6AP-E6-p53 dimeric ternary complex with p53-$NCP^{SHL+5.9}$ reveals steric clashes with the nucleosome. The dimeric ternary complex model, depicted in semi-transparent surface representation, is superimposed on two protomers of the $p53^{DBD}$ tetramer bound to the nucleosome. E6 and E6AP form several clashes with the nucleosome (arrows), including both DNA gyres and the histone face.

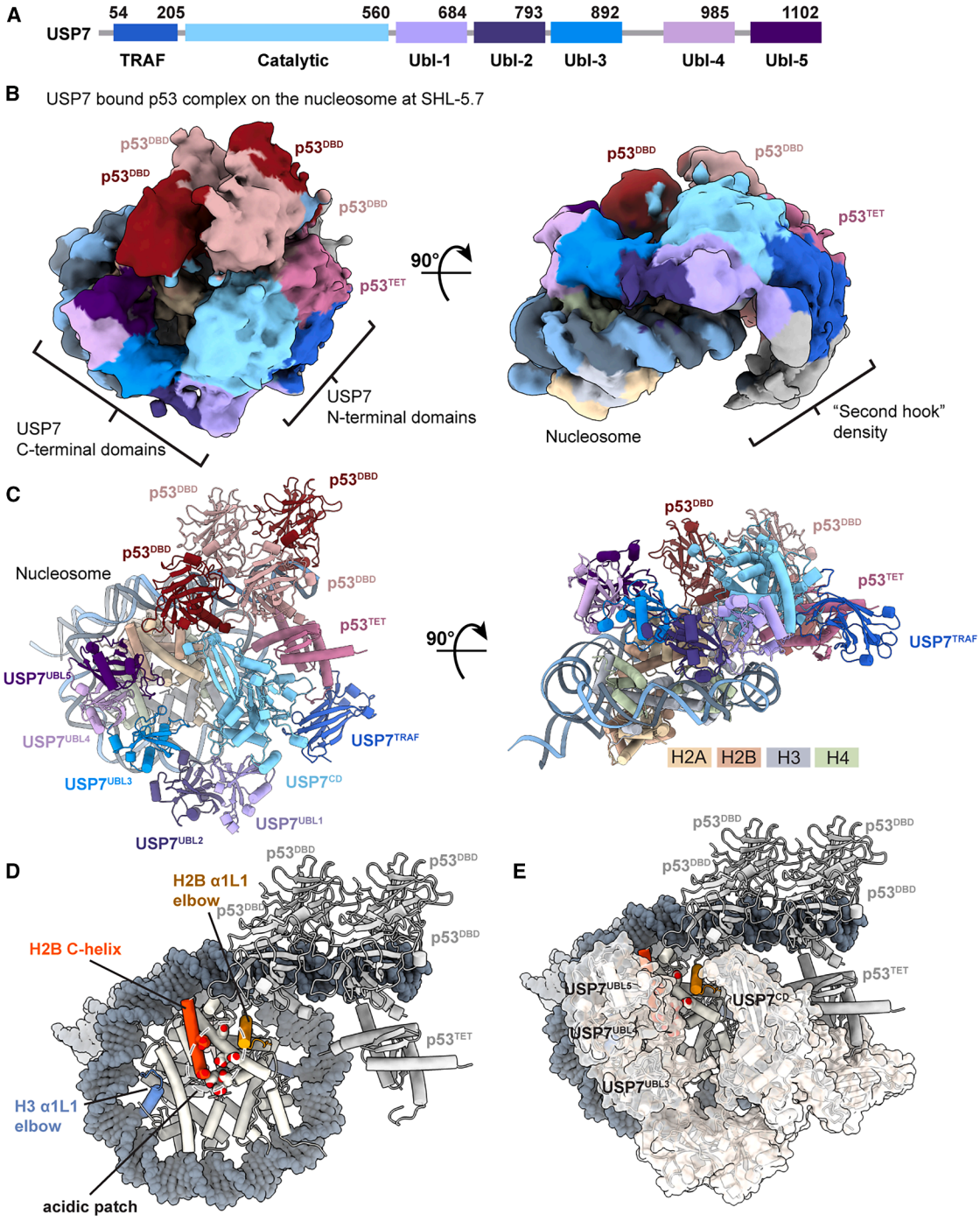

Figure 5. Cryo-EM structure of USP7^{FL}-p53-NCP$^{SHL-5.7}$ complex

(A) Domain organization of the deubiquitinase USP7.

(B) Cryo-EM density of the USP7^{FL}-p53-NCP$^{SHL-5.7}$ complex; p53^{DBD} is color-zoned in shades of light and dark red while p53^{TET} is in pink; domains of USP7 are shown according to domain map in (A). Histones are colored as indicated.

(C) Integrative atomic model of the complex.

(D) Protein interaction "hotspots" on the nucleosome from the integrative atomic model of USP7^{FL}-p53-NCP$^{SHL-5.7}$. USP7 is hidden for clarity. Regions of histones frequently involved in interactions with chromatin binding proteins are colored and indicated with a label. DNA, histones, and p53 protein are shown in different gray shades for clarity.

(E) The C-terminal UBL domains of USP7 make contacts with protein interaction hotspots on the nucleosome. The integrative atomic model of USP7^{FL}-p53-NCP$^{SHL-5.7}$ is shown as in (C). USP7 is depicted as semi-transparent surface representation.

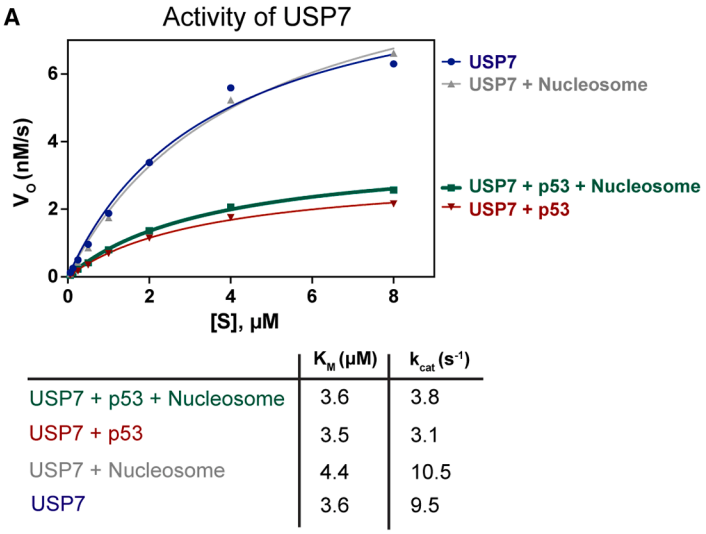

	K_M (μM)	k_{cat} (s^{-1})
USP7 + p53 + Nucleosome	3.6	3.8
USP7 + p53	3.5	3.1
USP7 + Nucleosome	4.4	10.5
USP7	3.6	9.5

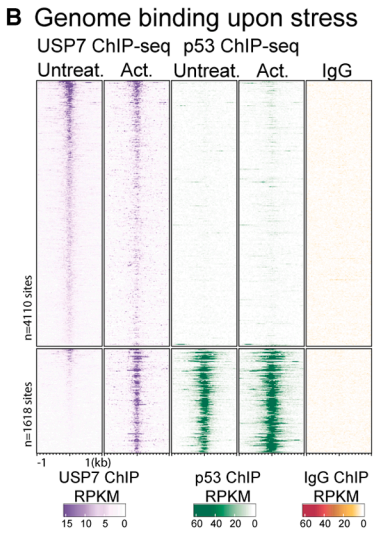

Figure 6. USP7 is functional and co-localizes with p53 on chromatin in cells

(A) Steady-state kinetic analysis of USP7 in complex with p53 and nucleosome indicates nucleosome compatibility of USP7 and an active DUB in the vicinity of nucleosome. The nucleosome used in the assay has the W601 sequence with p53 motif at SHL−5.7. The Michaelis-Menten constant (K_M) and k_{cat} were obtained by fitting the initial velocity (V_o) data for eight concentrations of the substrate Ub-rhodamine 110 (concentrations have been listed in Figure S18E). Data points are the mean of n = 3 measurements for USP7 plot. For the conditions involving a complex of USP7 with either p53 or nucleosome, as well as both p53 and nucleosome, data points are the mean of n = 2 measurements.

(B) USP7 binds to the genome (left), where upon p53 activation by cellular stress (4 h, doxorubicin 1 μM), USP7 binding increases at a subset of sites enriched for p53 binding (lower panels, log2 1.5-fold over immunoglobulin G [IgG] control).

are facing toward $USP7^{CD}$/ubiquitin and thus could be potential targets for deubiquitylation by nucleosome-engaged USP7. Additionally, our model places the $USP7^{CD}$ proximal to known ubiquitinated lysine residues in the flexible linker region between $p53^{DBD}$ and $p53^{TET}$ (K292), as well as residues within the TET itself (K351) and the C terminus of p53 (K357).[83,84] Owing to the flexible linkers within p53, we would expect these ubiquitination sites to be similarly accessible for nucleosome-engaged USP7.

USP7 activity is not impacted by the p53-nucleosome complex

The accessibility of the USP7 active site in the context of the nucleosome-bound p53 complex suggests that USP7 can be active when engaged with chromatin. USP7 is regulated by a "switching loop" mechanism where the misaligned catalytic triad (Cys223, His464, and Asp481) undergoes a conformational transition in complex with ubiquitin.[32]

To determine whether nucleosome binding interferes with ubiquitin substrate-binding and activation of the enzyme, we measured the activity of USP7 in complex with nucleosome-bound p53 using $NCP^{SHL-5.7}$. We qualitatively analyzed the deubiquitination capacity of USP7 using labeled tetra-ubiquitin chains (K-48 and K-63) in the presence of excess nucleosome ($NCP^{SHL-5.7}$) and p53 and found USP7 to be active on these substrates (Figure S17). We then performed steady-state deubiquitination assays using the fluorogenic minimal substrate ubiquitin-rhodamine 110 (Ub-rhodamine), monitoring the cleavage of the fluorescent label triggered by the DUB activity. Under these assay conditions, USP7 steady-state Michaelis-Menten parameters were determined as K_M: 3.6 μM and k_{cat}: 9.5 s^{-1}, respectively (Figure 6A). These values are in accordance with recently published data.[85] USP7 in the presence of p53 gave a k_{cat} and K_M of 3.1 s^{-1} and 3.5 μM, respectively. We then determined the activity of USP7 in complex with nucleosome-bound p53. We used USP7 (1 nM) incubated with excess of p53 (4 μM) and nucleosome (100 nM, p53 motif at $NCP^{SHL-5.7}$) for steady-state parameter determination. To ensure that the concentration of p53 and the nucleosome are indeed near saturation under our assay conditions, we kept the USP7 and Ub-rhodamine concentration constant and doubled the concentration of p53 or nucleosome in single measurements. This gave rise to near-identical USP7 activity traces (Figures S18A–S18D), as expected for near-saturation conditions. For USP7 activity in the presence of p53 and nucleosomes, we observed little change relative to the experiments done in the absence of nucleosomes, with a k_{cat} and K_M of 3.8 s^{-1} and 3.6 μM, respectively (Figure 6A). We concluded that USP7 activity for the Ub-rhodamine model substrate is not impacted by nucleosome binding and that the USP7 DUB remains largely functional when recruited to nucleosome-bound p53, in line with unobstructed access to p53 in our model.

USP7 and p53 co-localize on chromatin under basal and stress conditions

Given the direct and extensive interactions between USP7 and p53 in the nucleosome context induced upon DNA damage,[86] we next examined the binding preference of p53 and USP7 to chromatin in cells. We performed ChIP-seq on USP7 in mouse embryonic stem cells (mESCs) under normal conditions and upon doxorubicin treatment that activates p53 via stress

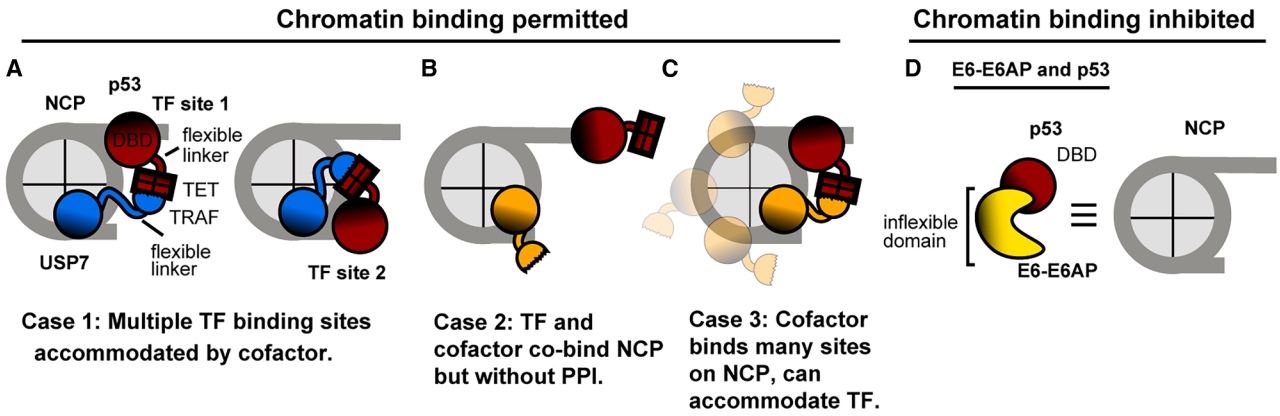

Figure 7. Proposed mechanisms of TF co-regulator binding to nucleosomes

Simultaneous chromatin binding by TF and co-regulator may be accomplished by three different schemes. Inhibition of chromatin binding, however, may be caused by the inflexibility of the co-regulator itself.

signaling pathways in cells (see Isbel et al.[15] for experimental conditions). Although p53, with its pioneering capabilities, can access its binding sites on both closed and open chromatin, the binding of p53 to chromatinized sites increases significantly upon stress-mediated activation.[12,15–17] We identified approximately 5,000 binding sites for USP7, with roughly a third overlapping with p53 binding in a stress-dependent manner (Figures 6B and S18L–S18N). USP7's non-overlapping binding sites are likely generated by USP7's interaction with other chromatin involved factors and histones.[35–43] Indeed, while there was little scaling in ChIP-seq signal between p53 and USP7 under non-stress conditions, USP7 binding scales very well with p53 binding under stress, arguing that the interaction at these sites is primarily due to the stress-dependent activation of p53 (Figure 6B). While we have previously noted p53 co-factor binding in particular chromatin environments,[15] this was not the case with USP7, with increased binding at p53 sites in both open and closed chromatin (Figure 6B). Thus, in the cellular context, we observed the stress-dependent recruitment of USP7 by p53 at chromatinized sites in line with the compatibility of USP7 to bind to chromatinized p53-binding sites *in vitro*. This is consistent with previously reported checkpoint-dependent binding and co-localization of USP7 and p53.[87] Together, these data argue that p53 recruits the nucleosome-compatible co-factor USP7 under stress and that USP7 appears well-tolerated in closed chromatin.

DISCUSSION

TFs engage binding sites on chromatin for gene activation, such as in response to cellular stress signals. These motifs are frequently situated in closed chromatin and are therefore difficult to access in a subset of the genome. Following TF binding, closed chromatin typically becomes open and accessible through the action of co-factors, requiring co-factors to engage pioneering TFs on or near nucleosomes and to drive the recruitment of the machinery required for chromatin opening and transcriptional activation. While TF binding to nucleosomal sites is increasingly better understood,[2,7] how co-factors engage TF/nucleosome complexes is not known. This is a substantial molecular recognition challenge, considering that the precise TF/nucleosome architecture varies as a function of the motif position.

We find that the E3 ubiquitin ligase E6-E6AP is incompatible with p53 binding on nucleosomes at two positions, while the E6-E6AP-p53 complex remains DNA bound in the absence of nucleosomes, albeit at a reduced affinity, compared with p53 alone. In a p53-dependent *in vitro* transcription system, where transcription of a chromatinized template was dependent on p53 and p300, the addition of E6 ablated transcription. This was assigned to the inability of p53 to direct p300 activity to nucleosomes in the presence of E6.[88] In the context of HPV pathogenesis, E6AP may therefore serve a dual role in degrading p53, a long-term solution that removes a potent apoptotic factor, and also inhibiting p53's ability to productively engage chromatin or other co-factors on nucleosomes.

USP7, on the other hand, engages p53 at its physiological site at the entry/exit site of the nucleosome at positions SHL−5.7 and SHL+5.9 in open and closed chromatin. Our structural studies illustrate that this is made possible through extensive protein-protein contacts between nucleosomes and p53. Complementary functional studies showed that p53 and USP7 also co-reside on chromatin in cells; yet in cells, USP7 can engage chromatin in the absence of p53, likely with the help of other nuclear binding partners.

As a more general model for how nucleosome/TF complexes recognize co-factors, we suggest that for those co-factors that can bind TFs on nucleosomes (e.g., p300, CBP, BAF, SIN3A/B, etc.), the co-factors must bind TFs in multiple different states depending on where the motif is located on the nucleosome. This may be best realized if the interaction between TFs and co-factors involves at least one binding domain being on a flexible linker (Figure 7A). In this scenario, the co-factor can also read out the different rotational and translational registers of a TF relative to the nucleosome and engage p53 at different sites on the nucleosome. When the co-factors bind the DBD directly, on the other hand, without being flexibly tethered, as is the case for E6-E6AP, this is expected to be more inhibitory for nucleosome binding, given the sterically crowded environment of the DBD

around the nucleosome. Hence, whether chromatin is repressive for co-factor binding, as well as the extent of the repressive behavior, likely depends on the co-factor interaction mode of the TF. The co-factor has to be able to reach the nucleosome-bound TF, which in turn can be present in different registers, sites, and orientations on the nucleosome (in the case of p53, see Figure 1G for three possible conformations p53 can assume). A single linker on the co-factor, however, is likely not sufficient to reach all possible TF orientations. Co-factor binding to TF/nucleosome complexes would hence be further facilitated by the ability of the co-factor to engage different epitopes on the histone, thereby occupying binding sites where the TF can be bound directly. Such multiple co-factor binding sites on nucleosomes were, for example, observed for p300[89,90] (Figure 7). Conversely, co-factors that reduce the TFs affinity for DNA, as in the case of E6-E6AP and p53, may be disproportionately affected by the obstacle that nucleosomes pose for DNA access, further reducing their ability to bind chromatin. Therefore, rather than merely being a principal barrier, chromatin may additionally serve as a filter to modulate co-factor access to nucleosome.

Limitations of the study

We demonstrate the nucleosome co-binding capability of p53 and two co-factors and generalize this capability to other TFs and transcriptional regulators. However, we do not account for the role of posttranslational modifications of histones or TFs, which may exert an important role in chromatin binding. While the E6-E6AP-p53 ternary complex did not bind nucleosomes at the two positions tested, it is conceivable that at other internal positions or linker-embedded sites, the co-factor could still be more or less excluded. The detailed measurements of position-dependent co-factor binding will warrant further study.

RESOURCE AVAILABILITY

Lead contact

Requests and correspondence should be addressed to the lead contact, Nicolas H. Thomä (nicolas.thoma@epfl.ch).

Materials availability

Materials are available upon request from Nicolas H. Thomä and with a materials transfer agreement with EPFL.

Data and code availability

- The electron microscopy (EM) density maps have been deposited in the Electron Microscopy Data Bank (EMD:53537, EMD:53478, EMD:53532, EMD:53534, EMD:53535, EMD:53536, EMD:53517, EMD:18809, and EMD:18810). Atomic models were deposited at the RCSB Protein Data Bank (PDB: 9R2Q, PDB: 9R04, PDB: 9R2M, PDB: 9R2P, PDB: 8R1F, and PDB: 8R1G, and PDB-IHM: 9A9W). In addition to our own datasets (deposited at GEO with ascension numbers GEO: GSE299056 and GEO: GSE299057, these datasets will become public upon publication) for ChIP-seq and Cut and Run experiments, we used public and previously published sequencing datasets for the ChIP-seq analysis (GEO accession identifiers GEO: GSM6038035, GEO: GSM 6038036, GEO: GSM6038037, GEO: GSM6038038, GEO: GSM 6038043, and GEO: GSM6038044). XL-MS data are available through the ProteomeXchange via the PRIDE database with the identifiers PRIDE: PXD054140 and PRIDE: PXD054141.
- Custom code was written for the p53-nucleosome clash analysis and has been deposited with the accession code (DOI): https://doi.org/10.5281/zenodo.15706014. The top 5 models from the TET domain docking have been deposited with the accession code (DOI): https://doi.org/10.5281/zenodo.15268030.
- Any additional information required to reanalyze the data reported in this paper is available from the lead contact upon request.

ACKNOWLEDGMENTS

We thank M. Schütz for laboratory management, organization, and assistance with manuscript editing. We are grateful to all Thomä and Schübeler lab members. We thank Ulrich Hassiepen from Novartis for his support and insightful discussions on the kinetic analysis. This work was supported by funding from the European Research Council (ERC), under the European Union's H2020 research program (NucEM, grant no. 884331); the Swiss National Science Foundation (SNF, grant no. 310030_301206 and 310030_214852); Krebsforschung (KFS, grant no. KFS-5933-08-2023); Novartis Research Foundation (to N.H.T.); the Novartis Freenovation (grant no. FN23-0000000514 to C. R.S.); the National Health and Medical Research Council CJ Martin Fellowship (APP1148380); the EU Horizon 2020 Research and Innovation Program under the Marie Sklodowska-Curie grant (grant no. 748760); the South Australian immunoGENomics Cancer Institute grant funding from the Australian Government; and the Sylvia and Charles Viertel Charitable Foundation Senior Medical Research Fellowship (to L.I.).

AUTHOR CONTRIBUTIONS

Conceptualization, D.C., C.R.S., D.S., A.K.M., and N.H.T.; methodology, D.C., C.R.S., D.S., A.K.M., and N.H.T.; investigation, D.C., C.R.S., L.I., G.K., J.W., S. C., L.K., J.S., Z.K., L.S., R.S.G., and A.K.M.; funding acquisition, D.S. and N.H. T.; writing, D.C., C.R.S., L.I., D.S., and N.H.T.

DECLARATION OF INTERESTS

The authors declare no competing interests.

STAR★METHODS

Detailed methods are provided in the online version of this paper and include the following:

- KEY RESOURCES TABLE
- EXPERIMENTAL MODEL AND STUDY PARTICIPANT DETAILS
- METHOD DETAILS
  - Expression, purification and reconstitution of histone octamers
  - DNA purification and reconstitution of nucleosome
  - Large scale nucleosome reconstitution for cryo-EM
  - Small scale nucleosome reconstitution for deubiquitination assays, EMSA and FIDA
  - Protein expression and purification
  - SeEN-seq library preparation
  - Generation of linker SeENseq pool
  - SeEN-seq assay
  - CUT & RUN
  - Generation of double-stranded oligonucleotides
  - Size-exclusion chromatography (SEC)
  - SEC-MALS
  - Mass photometry
  - Fluorescence polarization
  - XL-MS
  - Crosslink- and density-guided docking simulations
  - Cryo-EM sample preparation
  - Cryo-EM data collection (see Table 1 Statistics for details)
  - Cryo-EM image processing
  - Model building and refinement
  - Simulation of p53 nucleosome clash scores
  - ChIP-seq
  - Deubiquitination of ubiquitin chains

- Deubiquitination of minimal substrate Ub-rhodamine 110
- EMSA
- FIDA measurements

- QUANTIFICATION AND STATISTICAL ANALYSIS
  - SeEN-seq analysis
  - CUT & RUN analysis
  - Fluorescence polarization analysis
  - XL-MS analysis
  - ChIP-seq analysis
  - Deubiquitination of minimal substrate Ub-rhodamine 110 - analysis
  - EMSA quantification

SUPPLEMENTAL INFORMATION

Supplemental information can be found online at https://doi.org/10.1016/j.molcel.2025.06.027.

Received: October 11, 2024
Revised: May 7, 2025
Accepted: June 30, 2025
Published: July 25, 2025

REFERENCES

1. Bilokapic, S., Strauss, M., and Halic, M. (2018). Structural rearrangements of the histone octamer translocate DNA. Nat. Commun. *9*, 1330. https://doi.org/10.1038/s41467-018-03677-z.
2. Michael, A.K., and Thomä, N.H. (2021). Reading the chromatinized genome. Cell *184*, 3599–3611. https://doi.org/10.1016/j.cell.2021.05.029.
3. Bai, Y., and Zhou, B.-R. (2021). Structures of Native-like Nucleosomes: One Step Closer toward Understanding the Structure and Function of Chromatin. J. Mol. Biol. *433*, 166648. https://doi.org/10.1016/j.jmb.2020.09.007.
4. Mirny, L.A. (2010). Nucleosome-mediated cooperativity between transcription factors. Proc. Natl. Acad. Sci. USA *107*, 22534–22539. https://doi.org/10.1073/pnas.0913805107.
5. Sekine, S.I., Ehara, H., Kujirai, T., and Kurumizaka, H. (2024). Structural perspectives on transcription in chromatin. Trends Cell Biol. *34*, 211–224. https://doi.org/10.1016/j.tcb.2023.07.011.
6. Luger, K., Mäder, A.W., Richmond, R.K., Sargent, D.F., and Richmond, T.J. (1997). Crystal structure of the nucleosome core particle at 2.8 Å resolution. Nature *389*, 251–260. https://doi.org/10.1038/38444.
7. Carminati, M., Vecchia, L., Stoos, L., and Thomä, N.H. (2024). Pioneer factors: Emerging rules of engagement for transcription factors on chromatinized DNA. Curr. Opin. Struct. Biol. *88*, 102875. https://doi.org/10.1016/j.sbi.2024.102875.
8. Farnung, L., Vos, S.M., Wigge, C., and Cramer, P. (2017). Nucleosome–Chd1 structure and implications for chromatin remodelling. Nature *550*, 539–542. https://doi.org/10.1038/nature24046.
9. Michael, A.K., Grand, R.S., Isbel, L., Cavadini, S., Kozicka, Z., Kempf, G., Bunker, R.D., Schenk, A.D., Graff-Meyer, A., Pathare, G.R., et al. (2020). Mechanisms of OCT4-SOX2 motif readout on nucleosomes. Science *368*, 1460–1465. https://doi.org/10.1126/science.abb0074.
10. Donovan, B.T., Chen, H., Eek, P., Meng, Z., Jipa, C., Tan, S., Bai, L., and Poirier, M.G. (2023). Basic helix-loop-helix pioneer factors interact with the histone octamer to invade nucleosomes and generate nucleosome-depleted regions. Mol. Cell *83*, 1251–1263.e6. https://doi.org/10.1016/j.molcel.2023.03.006.
11. Levine, A.J. (1997). p53, the Cellular Gatekeeper for Growth and Division. Cell *88*, 323–331. https://doi.org/10.1016/S0092-8674(00)81871-1.
12. Younger, S.T., and Rinn, J.L. (2017). p53 regulates enhancer accessibility and activity in response to DNA damage. Nucleic Acids Res. *45*, 9889–9900. https://doi.org/10.1093/nar/gkx577.
13. Hollstein, M., Rice, K., Greenblatt, M.S., Soussi, T., Fuchs, R., Sørlie, T., Hovig, E., Smith-Sørensen, B., Montesano, R., and Harris, C.C. (1994). Database of p53 gene somatic mutations in human tumors and cell lines. Nucleic Acids Res. *22*, 3551–3555.
14. Kastenhuber, E.R., and Lowe, S.W. (2017). Putting p53 in Context. Cell *170*, 1062–1078. https://doi.org/10.1016/j.cell.2017.08.028.
15. Isbel, L., Iskar, M., Durdu, S., Weiss, J., Grand, R.S., Hietter-Pfeiffer, E., Kozicka, Z., Michael, A.K., Burger, L., Thomä, N.H., et al. (2023). Readout of histone methylation by Trim24 locally restricts chromatin opening by p53. Nat. Struct. Mol. Biol. *30*, 948–957. https://doi.org/10.1038/s41594-023-01021-8.
16. Sammons, M.A., Zhu, J., Drake, A.M., and Berger, S.L. (2015). TP53 engagement with the genome occurs in distinct local chromatin environments via pioneer factor activity. Genome Res. *25*, 179–188. https://doi.org/10.1101/gr.181883.114.
17. Tonelli, C., Morelli, M.J., Bianchi, S., Rotta, L., Capra, T., Sabò, A., Campaner, S., and Amati, B. (2015). Genome-wide analysis of p53 transcriptional programs in B cells upon exposure to genotoxic stress in vivo. Oncotarget *6*, 24611–24626. https://doi.org/10.18632/oncotarget.5232.
18. Nishimura, M., Takizawa, Y., Nozawa, K., and Kurumizaka, H. (2022). Structural basis for p53 binding to its nucleosomal target DNA sequence. PNAS Nexus *1*, pgac177. https://doi.org/10.1093/pnasnexus/pgac177.
19. Scheffner, M., Huibregtse, J.M., Vierstra, R.D., and Howley, P.M. (1993). The HPV-16 E6 and E6-AP complex functions as a ubiquitin-protein ligase in the ubiquitination of p53. Cell *75*, 495–505. https://doi.org/10.1016/0092-8674(93)90384-3.
20. Rodriguez, M.S., Desterro, J.M.P., Lain, S., Lane, D.P., and Hay, R.T. (2000). Multiple C-Terminal Lysine Residues Target p53 for Ubiquitin-Proteasome-Mediated Degradation. Mol. Cell. Biol. *20*, 8458–8467. https://doi.org/10.1128/MCB.20.22.8458-8467.2000.
21. Everett, R.D., Meredith, M., Orr, A., Cross, A., Kathoria, M., and Parkinson, J. (1997). A novel ubiquitin-specific protease is dynamically associated with the PML nuclear domain and binds to a herpesvirus regulatory protein. EMBO J. *16*, 1519–1530. https://doi.org/10.1093/emboj/16.7.1519.
22. Rong, X., Rao, J., Li, D., Jing, Q., Lu, Y., and Ji, Y. (2019). TRIM69 inhibits cataractogenesis by negatively regulating p53. Redox Biol. *22*, 101157. https://doi.org/10.1016/j.redox.2019.101157.
23. Zhou, Z., Ji, Z., Wang, Y., Li, J., Cao, H., Zhu, H.H., and Gao, W.-Q. (2014). TRIM59 Is Up-regulated in Gastric Tumors, Promoting Ubiquitination and Degradation of p53. Gastroenterology *147*, 1043–1054. https://doi.org/10.1053/j.gastro.2014.07.021.
24. Vogelstein, B., Lane, D., and Levine, A.J. (2000). Surfing the p53 network. Nature *408*, 307–310. https://doi.org/10.1038/35042675.
25. Oren, M. (2003). Decision making by p53: life, death and cancer. Cell Death Differ. *10*, 431–442. https://doi.org/10.1038/sj.cdd.4401183.
26. Wade, M., Li, Y.-C., and Wahl, G.M. (2013). MDM2, MDMX and p53 in oncogenesis and cancer therapy. Nat. Rev. Cancer *13*, 83–96. https://doi.org/10.1038/nrc3430.
27. Qi, S.-M., Cheng, G., Cheng, X.-D., Xu, Z., Xu, B., Zhang, W.-D., and Qin, J.-J. (2020). Targeting USP7-Mediated Deubiquitination of MDM2/MDMX-p53 Pathway for Cancer Therapy: Are We There Yet? Front. Cell Dev. Biol. *8*, 233. https://doi.org/10.3389/fcell.2020.00233.
28. Li, M., Brooks, C.L., Kon, N., and Gu, W. (2004). A Dynamic Role of HAUSP in the p53-Mdm2 Pathway. Mol. Cell *13*, 879–886. https://doi.org/10.1016/S1097-2765(04)00157-1.
29. Cummins, J.M., Rago, C., Kohli, M., Kinzler, K.W., Lengauer, C., and Vogelstein, B. (2004). Disruption of HAUSP gene stabilizes p53. Nature *428*, 1–2. https://doi.org/10.1038/nature02501.
30. Cummins, J.M., and Vogelstein, B. (2004). HAUSP is required for p53 destabilization. Cell Cycle *3*, 689–692. https://doi.org/10.4161/cc.3.6.924.

31. Meulmeester, E., Maurice, M.M., Boutell, C., Teunisse, A.F.A.S., Ovaa, H., Abraham, T.E., Dirks, R.W., and Jochemsen, A.G. (2005). Loss of HAUSP-Mediated Deubiquitination Contributes to DNA Damage-Induced Destabilization of Hdmx and Hdm2. Mol. Cell *18*, 565–576. https://doi.org/10.1016/j.molcel.2005.04.024.

32. Rougé, L., Bainbridge, T.W., Kwok, M., Tong, R., Di Lello, P., Wertz, I.E., Maurer, T., Ernst, J.A., and Murray, J. (2016). Molecular Understanding of USP7 Substrate Recognition and C-Terminal Activation. Structure *24*, 1335–1345. https://doi.org/10.1016/j.str.2016.05.020.

33. Sheng, Y., Saridakis, V., Sarkari, F., Duan, S., Wu, T., Arrowsmith, C.H., and Frappier, L. (2006). Molecular recognition of p53 and MDM2 by USP7/HAUSP. Nat. Struct. Mol. Biol. *13*, 285–291. https://doi.org/10.1038/nsmb1067.

34. Pozhidaeva, A., and Bezsonova, I. (2019). USP7: structure, substrate specificity, and inhibition. DNA Repair (Amst) *76*, 30–39. https://doi.org/10.1016/j.dnarep.2019.02.005.

35. Wu, H.-T., Kuo, Y.-C., Hung, J.-J., Huang, C.-H., Chen, W.-Y., Chou, T.-Y., Chen, Y., Chen, Y.-J., Chen, Y.-J., Cheng, W.-C., et al. (2016). K63-polyubiquitinated HAUSP deubiquitinates HIF-1α and dictates H3K56 acetylation promoting hypoxia-induced tumour progression. Nat. Commun. *7*, 13644. https://doi.org/10.1038/ncomms13644.

36. van der Horst, A., de Vries-Smits, A.M.M., Brenkman, A.B., van Triest, M. H., van den Broek, N., Colland, F., Maurice, M.M., and Burgering, B.M.T. (2006). FOXO4 transcriptional activity is regulated by monoubiquitination and USP7/HAUSP. Nat. Cell Biol. *8*, 1064–1073. https://doi.org/10.1038/ncb1469.

37. Nie, L., Wang, C., Liu, X., Teng, H., Li, S., Huang, M., Feng, X., Pei, G., Hang, Q., Zhao, Z., et al. (2022). USP7 substrates identified by proteomics analysis reveal the specificity of USP7. Genes Dev. *36*, 1016–1030. https://doi.org/10.1101/gad.349848.122.

38. Yamaguchi, L., Nishiyama, A., Misaki, T., Johmura, Y., Ueda, J., Arita, K., Nagao, K., Obuse, C., and Nakanishi, M. (2017). Usp7-dependent histone H3 deubiquitylation regulates maintenance of DNA methylation. Sci. Rep. *7*, 55. https://doi.org/10.1038/s41598-017-00136-5.

39. van der Knaap, J.A., Kumar, B.R.P., Moshkin, Y.M., Langenberg, K., Krijgsveld, J., Heck, A.J.R., Karch, F., and Verrijzer, C.P. (2005). GMP Synthetase Stimulates Histone H2B Deubiquitylation by the Epigenetic Silencer USP7. Mol. Cell *17*, 695–707. https://doi.org/10.1016/j.molcel.2005.02.013.

40. Valles, G.J., Bezsonova, I., Woodgate, R., and Ashton, N.W. (2020). USP7 Is a Master Regulator of Genome Stability. Front. Cell Dev. Biol. *8*, 717. https://doi.org/10.3389/fcell.2020.00717.

41. Jagannathan, M., Nguyen, T., Gallo, D., Luthra, N., Brown, G.W., Saridakis, V., and Frappier, L. (2014). A Role for USP7 in DNA Replication. Mol. Cell. Biol. *34*, 132–145. https://doi.org/10.1128/MCB.00639-13.

42. He, J., Zhu, Q., Wani, G., Sharma, N., Han, C., Qian, J., Pentz, K., Wang, Q.E., and Wani, A.A. (2014). Ubiquitin-specific Protease 7 Regulates Nucleotide Excision Repair through Deubiquitinating XPC Protein and Preventing XPC Protein from Undergoing Ultraviolet Light-induced and VCP/p97 Protein-regulated Proteolysis. J. Biol. Chem. *289*, 27278–27289. https://doi.org/10.1074/jbc.M114.589812.

43. Schwertman, P., Lagarou, A., Dekkers, D.H.W., Raams, A., van der Hoek, A.C., Laffeber, C., Hoeijmakers, J.H.J., Demmers, J.A.A., Fousteri, M., Vermeulen, W., et al. (2012). UV-sensitive syndrome protein UVSSA recruits USP7 to regulate transcription-coupled repair. Nat. Genet. *44*, 598–602. https://doi.org/10.1038/ng.2230.

44. Wang, Q., Ma, S., Song, N., Li, X., Liu, L., Yang, S., Ding, X., Shan, L., Zhou, X., Su, D., et al. (2016). Stabilization of histone demethylase PHF8 by USP7 promotes breast carcinogenesis. J. Clin. Invest. *126*, 2205–2220. https://doi.org/10.1172/JCI85747.

45. Aloni-Grinstein, R., Charni-Natan, M., Solomon, H., and Rotter, V. (2018). p53 and the Viral Connection: Back into the Future ‡. Cancers *10*, 178. https://doi.org/10.3390/cancers10060178.

46. Lemak, A., Yee, A., Bezsonova, I., Dhe-Paganon, S., and Arrowsmith, C. H. (2011). Zn-binding AZUL domain of human ubiquitin protein ligase Ube3A. J. Biomol. NMR *51*, 185–190. https://doi.org/10.1007/s10858-011-9552-y.

47. Nawaz, Z., Lonard, D.M., Smith, C.L., Lev-Lehman, E., Tsai, S.Y., Tsai, M.J., and O'Malley, B.W. (1999). The Angelman Syndrome-Associated Protein, E6-AP, Is a Coactivator for the Nuclear Hormone Receptor Superfamily. Mol. Cell. Biol. *19*, 1182–1189. https://doi.org/10.1128/MCB.19.2.1182.

48. Louria-Hayon, I., Alsheich-Bartok, O., Levav-Cohen, Y., Silberman, I., Berger, M., Grossman, T., Matentzoglu, K., Jiang, Y.H., Muller, S., Scheffner, M., et al. (2009). E6AP promotes the degradation of the PML tumor suppressor. Cell Death Differ. *16*, 1156–1166. https://doi.org/10.1038/cdd.2009.31.

49. Shimoji, T., Murakami, K., Sugiyama, Y., Matsuda, M., Inubushi, S., Nasu, J., Shirakura, M., Suzuki, T., Wakita, T., Kishino, T., et al. (2009). Identification of annexin A1 as a novel substrate for E6AP-mediated ubiquitylation. J. Cell. Biochem. *106*, 1123–1135. https://doi.org/10.1002/jcb.22096.

50. Wang, Y., Liu, X., Zhou, L., Duong, D., Bhuripanyo, K., Zhao, B., Zhou, H., Liu, R., Bi, Y., Kiyokawa, H., et al. (2017). Identifying the ubiquitination targets of E6AP by orthogonal ubiquitin transfer. Nat. Commun. *8*, 2232. https://doi.org/10.1038/s41467-017-01974-7.

51. Kishino, T., Lalande, M., and Wagstaff, J. (1997). UBE3A/E6-AP mutations cause Angelman syndrome. Nat. Genet. *15*, 70–73. https://doi.org/10.1038/ng0197-70.

52. Gentile, J.K., Tan, W.-H., Horowitz, L.T., Bacino, C.A., Skinner, S.A., Barbieri-Welge, R., Bauer-Carlin, A., Beaudet, A.L., Bichell, T.J., Lee, H.-S., et al. (2010). A neurodevelopmental survey of Angelman syndrome with genotype-phenotype correlations. J. Dev. Behav. Pediatr. *31*, 592–601. https://doi.org/10.1097/DBP.0b013e3181ee408e.

53. Noor, A., Dupuis, L., Mittal, K., Lionel, A.C., Marshall, C.R., Scherer, S.W., Stockley, T., Vincent, J.B., Mendoza-Londono, R., and Stavropoulos, D.J. (2015). 15q11.2 Duplication Encompassing Only the UBE3A Gene Is Associated with Developmental Delay and Neuropsychiatric Phenotypes. Hum. Mutat. *36*, 689–693. https://doi.org/10.1002/humu.22800.

54. Hafner, A., Bulyk, M.L., Jambhekar, A., and Lahav, G. (2019). The multiple mechanisms that regulate p53 activity and cell fate. Nat. Rev. Mol. Cell Biol. *20*, 199–210. https://doi.org/10.1038/s41580-019-0110-x.

55. Meers, M.P., Bryson, T.D., Henikoff, J.G., and Henikoff, S. (2019). Improved CUT&RUN chromatin profiling tools. eLife *8*, e46314. https://doi.org/10.7554/eLife.46314.

56. Zentner, G.E., and Henikoff, S. (2012). Surveying the epigenomic landscape, one base at a time. Genome Biol. *13*, 250. https://doi.org/10.1186/gb-2012-13-10-250.

57. Jeffrey, P.D., Gorina, S., and Pavletich, N.P. (1995). Crystal structure of the tetramerization domain of the p53 tumor suppressor at 1.7 angstroms. Science *267*, 1498–1502. https://doi.org/10.1126/science.7878469.

58. Kitayner, M., Rozenberg, H., Kessler, N., Rabinovich, D., Shaulov, L., Haran, T.E., and Shakked, Z. (2006). Structural Basis of DNA Recognition by p53 Tetramers. Mol. Cell *22*, 741–753. https://doi.org/10.1016/j.molcel.2006.05.015.

59. Yu, X., and Buck, M.J. (2019). Defining TP53 pioneering capabilities with competitive nucleosome binding assays. Genome Res. *29*, 107–115. https://doi.org/10.1101/gr.234104.117.

60. Nishimura, M., Arimura, Y., Nozawa, K., and Kurumizaka, H. (2020). Linker DNA and histone contributions in nucleosome binding by p53. J. Biochem. *168*, 669–675. https://doi.org/10.1093/jb/mvaa081.

61. Wilson, P.D., Yu, X., Handelmann, C.R., and Buck, M.J. (2025). Nucleosome binding by TP53, TP63, and TP73 is determined by the composition, accessibility, and helical orientation of their binding sites. Genome Res. *35*, 404–416. https://doi.org/10.1101/gr.279541.124.

62. Fornes, O., Castro-Mondragon, J.A., Khan, A., van der Lee, R., Zhang, X., Richmond, P.A., Modi, B.P., Correard, S., Gheorghe, M., Baranašić, D., et al. (2020). JASPAR 2020: update of the open-access database of transcription factor binding profiles. Nucleic Acids Res. *48*, D87–D92. https://doi.org/10.1093/nar/gkz1001.

63. Lowary, P.T., and Widom, J. (1998). New DNA sequence rules for high affinity binding to histone octamer and sequence-directed nucleosome positioning. J. Mol. Biol. *276*, 19–42. https://doi.org/10.1006/jmbi.1997.1494.

64. Joerger, A.C., and Fersht, A.R. (2007). Structural Biology of the Tumor Suppressor p53 and Cancer-Associated Mutants. Academic Press. Adv. Cancer Res. *97*, 1–23. https://doi.org/10.1016/S0065-230X(06)97001-8.

65. Guiley, K.Z., and Shokat, K.M. (2023). A Small Molecule Reacts with the p53 Somatic Mutant Y220C to Rescue Wild-type Thermal Stability. Cancer Discov. *13*, 56–69. https://doi.org/10.1158/2159-8290.CD-22-0381.

66. Balourdas, D.-I., Markl, A.M., Krämer, A., Settanni, G., and Joerger, A.C. (2024). Structural basis of p53 inactivation by cavity-creating cancer mutations and its implications for the development of mutant p53 reactivators. Cell Death Dis. *15*, 408. https://doi.org/10.1038/s41419-024-06739-x.

67. Kastner, B., Fischer, N., Golas, M.M., Sander, B., Dube, P., Boehringer, D., Hartmuth, K., Deckert, J., Hauer, F., Wolf, E., et al. (2008). GraFix: sample preparation for single-particle electron cryomicroscopy. Nat. Methods *5*, 53–55. https://doi.org/10.1038/nmeth1139.

68. Stark, H. (2010). GraFix: Stabilization of fragile macromolecular complexes for single particle cryo-EM. Methods Enzymol. *481*, 109–126. https://doi.org/10.1016/S0076-6879(10)81005-5.

69. Martinez-Zapien, D., Ruiz, F.X., Poirson, J., Mitschler, A., Ramirez, J., Forster, A., Cousido-Siah, A., Masson, M., Vande Pol, S.V., Podjarny, A., et al. (2016). Structure of the E6/E6AP/p53 complex required for HPV-mediated degradation of p53. Nature *529*, 541–545. https://doi.org/10.1038/nature16481.

70. Wang, J.C.K., Baddock, H.T., Mafi, A., Foe, I.T., Bratkowski, M., Lin, T.-Y., Jensvold, Z.D., Preciado López, M., Stokoe, D., Eaton, D., et al. (2024). Structure of the p53 degradation complex from HPV16. Nat. Commun. *15*, 1842. https://doi.org/10.1038/s41467-024-45920-w.

71. Wang, Z., Fan, F., Li, Z., Ye, F., Wang, Q., Gao, R., Qiu, J., Lv, Y., Lin, M., Xu, W., et al. (2024). Structural insights into the functional mechanism of the ubiquitin ligase E6AP. Nat. Commun. *15*, 3531. https://doi.org/10.1038/s41467-024-47586-w.

72. Davison, T.S., Nie, X., Ma, W., Lin, Y., Kay, C., Benchimol, S., and Arrowsmith, C.H. (2001). Structure and functionality of a designed p53 dimer. J. Mol. Biol. *307*, 605–617. https://doi.org/10.1006/jmbi.2001.4450.

73. Ho, W.C., Fitzgerald, M.X., and Marmorstein, R. (2006). Structure of the p53 core domain dimer bound to DNA. J. Biol. Chem. *281*, 20494–20502. https://doi.org/10.1074/jbc.M603634200.

74. Chen, Y., Dey, R., and Chen, L. (2010). Crystal Structure of the p53 Core Domain Bound to a Full Consensus Site as a Self-Assembled Tetramer. Structure *18*, 246–256. https://doi.org/10.1016/j.str.2009.11.011.

75. Faesen, A.C., Dirac, A.M.G., Shanmugham, A., Ovaa, H., Perrakis, A., and Sixma, T.K. (2011). Mechanism of USP7/HAUSP Activation by Its C-Terminal Ubiquitin-like Domain and Allosteric Regulation by GMP-Synthetase. Mol. Cell *44*, 147–159. https://doi.org/10.1016/j.molcel.2011.06.034.

76. Fernández-Montalván, A., Bouwmeester, T., Joberty, G., Mader, R., Mahnke, M., Pierrat, B., Schlaeppi, J.-M., Worpenberg, S., and Gerhartz, B. (2007). Biochemical characterization of USP7 reveals post-translational modification sites and structural requirements for substrate processing and subcellular localization. FEBS Journal *274*, 4256–4270. https://doi.org/10.1111/j.1742-4658.2007.05952.x.

77. Hu, M., Gu, L., Li, M., Jeffrey, P.D., Gu, W., and Shi, Y. (2006). Structural Basis of Competitive Recognition of p53 and MDM2 by HAUSP/USP7: Implications for the Regulation of the p53–MDM2 Pathway. PLoS Biol. *4*, e27. https://doi.org/10.1371/journal.pbio.0040027.

78. Saridakis, V., Sheng, Y., Sarkari, F., Holowaty, M.N., Shire, K., Nguyen, T., Zhang, R.G., Liao, J., Lee, W., Edwards, A.M., et al. (2005). Structure of the p53 binding domain of HAUSP/USP7 bound to Epstein-Barr nuclear antigen 1 implications for EBV-mediated immortalization. Mol. Cell *18*, 25–36. https://doi.org/10.1016/j.molcel.2005.02.029.

79. Hu, M., Li, P., Li, M., Li, W., Yao, T., Wu, J.-W., Gu, W., Cohen, R.E., and Shi, Y. (2002). Crystal Structure of a UBP-Family Deubiquitinating Enzyme in Isolation and in Complex with Ubiquitin Aldehyde. Cell *111*, 1041–1054. https://doi.org/10.1016/S0092-8674(02)01199-6.

80. Cheng, J., Yang, H., Fang, J., Ma, L., Gong, R., Wang, P., Li, Z., and Xu, Y. (2015). Molecular mechanism for USP7-mediated DNMT1 stabilization by acetylation. Nat. Commun. *6*, 7023. https://doi.org/10.1038/ncomms8023.

81. McGinty, R.K., and Tan, S. (2021). Principles of nucleosome recognition by chromatin factors and enzymes. Curr. Opin. Struct. Biol. *71*, 16–26. https://doi.org/10.1016/j.sbi.2021.05.006.

82. Chan, W.M., Mak, M.C., Fung, T.K., Lau, A., Siu, W.Y., and Poon, R.Y.C. (2006). Ubiquitination of p53 at Multiple Sites in the DNA-Binding Domain. Mol. Cancer Res. *4*, 15–25. https://doi.org/10.1158/1541-7786.MCR-05-0097.

83. Lee, E.-W., Lee, M.-S., Camus, S., Ghim, J., Yang, M.-R., Oh, W., Ha, N.-C., Lane, D.P., and Song, J. (2009). Differential regulation of p53 and p21 by MKRN1 E3 ligase controls cell cycle arrest and apoptosis. EMBO J. *28*, 2100–2113. https://doi.org/10.1038/emboj.2009.164.

84. Kruse, J.-P., and Gu, W. (2009). MSL2 Promotes Mdm2-independent Cytoplasmic Localization of p53. J. Biol. Chem. *284*, 3250–3263. https://doi.org/10.1074/jbc.M805658200.

85. Keijzer, N., Priyanka, A., Stijf-Bultsma, Y., Fish, A., Gersch, M., and Sixma, T.K. (2024). Variety in the USP deubiquitinase catalytic mechanism. Life Sci. Alliance *7*, e202302533. https://doi.org/10.26508/lsa.202302533.

86. Khoronenkova, S.V., Dianova, I.I., Ternette, N., Kessler, B.M., Parsons, J. L., and Dianov, G.L. (2012). ATM-Dependent Downregulation of USP7/HAUSP by PPM1G Activates p53 Response to DNA Damage. Mol. Cell *45*, 801–813. https://doi.org/10.1016/j.molcel.2012.01.021.

87. Liu, J., Cao, L., Wang, Y., Zou, Y., Guo, Q., Chen, S., Jiang, B., Wu, X., Zheng, L., Zhang, S., et al. (2024). The phosphorylation-deubiquitination positive feedback loop of the CHK2-USP7 axis stabilizes p53 under oxidative stress. Cell Rep. *43*, 114366. https://doi.org/10.1016/j.celrep.2024.114366.

88. Thomas, M.C., and Chiang, C.-M. (2005). E6 Oncoprotein Represses p53-Dependent Gene Activation via Inhibition of Protein Acetylation Independently of Inducing p53 Degradation. Mol. Cell *17*, 251–264. https://doi.org/10.1016/j.molcel.2004.12.016.

89. Kikuchi, M., Morita, S., Wakamori, M., Sato, S., Uchikubo-Kamo, T., Suzuki, T., Dohmae, N., Shirouzu, M., and Umehara, T. (2023). Epigenetic mechanisms to propagate histone acetylation by p300/CBP. Nat. Commun. *14*, 4103. https://doi.org/10.1038/s41467-023-39735-4.

90. Hatazawa, S., Liu, J., Takizawa, Y., Zandian, M., Negishi, L., Kutateladze, T.G., and Kurumizaka, H. (2022). Structural basis for binding diversity of acetyltransferase p300 to the nucleosome. iScience *25*, 104563. https://doi.org/10.1016/j.isci.2022.104563.

91. Liu, F., Lössl, P., Scheltema, R., Viner, R., and Heck, A.J.R. (2017). Optimized fragmentation schemes and data analysis strategies for proteome-wide cross-link identification. Nat. Commun. *8*, 15473. https://doi.org/10.1038/ncomms15473.

92. Schenk, A.D., Cavadini, S., Thomä, N.H., and Genoud, C. (2020). Live Analysis and Reconstruction of Single-Particle Cryo-Electron Microscopy Data with CryoFLARE. J. Chem. Inf. Model. *60*, 2561–2569. https://doi.org/10.1021/acs.jcim.9b01102.

93. Zivanov, J., Nakane, T., Forsberg, B.O., Kimanius, D., Hagen, W.J., Lindahl, E., and Scheres, S.H. (2018). New tools for automated high-resolution cryo-EM structure determination in RELION-3. eLife *7*, e42166. https://doi.org/10.7554/eLife.42166.

94. Punjani, A., Rubinstein, J.L., Fleet, D.J., and Brubaker, M.A. (2017). CryoSPARC: Algorithms for rapid unsupervised cryo-EM structure determination. Nat. Methods *14*, 290–296. https://doi.org/10.1038/nmeth.4169.

95. Pettersen, E.F., Goddard, T.D., Huang, C.C., Meng, E.C., Couch, G.S., Croll, T.I., Morris, J.H., and Ferrin, T.E. (2021). UCSF ChimeraX: Structure visualization for researchers, educators, and developers. Protein Sci. *30*, 70–82. https://doi.org/10.1002/pro.3943.

96. Emsley, P., and Cowtan, K. (2004). Coot: Model-building tools for molecular graphics. Acta Crystallogr. D Biol. Crystallogr. *60*, 2126–2132. https://doi.org/10.1107/S0907444904019158.

97. Croll, T.I. (2018). ISOLDE: A physically realistic environment for model building into low-resolution electron-density maps. Acta Crystallogr. D Struct. Biol. *74*, 519–530. https://doi.org/10.1107/S2059798318002425.

98. Jumper, J., Evans, R., Pritzel, A., Green, T., Figurnov, M., Ronneberger, O., Tunyasuvunakool, K., Bates, R., Žídek, A., Potapenko, A., et al. (2021). Highly accurate protein structure prediction with AlphaFold. Nature *596*, 583–589. https://doi.org/10.1038/s41586-021-03819-2.

99. Adams, P.D., Afonine, P.V., Bunkóczi, G., Chen, V.B., Davis, I.W., Echols, N., Headd, J.J., Hung, L.W., Kapral, G.J., Grosse-Kunstleve, R.W., et al. (2010). PHENIX: A comprehensive Python-based system for macromolecular structure solution. Acta Crystallogr. D Biol. Crystallogr. *66*, 213–221. https://doi.org/10.1107/S0907444909052925.

100. Chen, V.B., Arendall, W.B., Headd, J.J., Keedy, D.A., Immormino, R.M., Kapral, G.J., Murray, L.W., Richardson, J.S., and Richardson, D.C. (2010). MolProbity: All-atom structure validation for macromolecular crystallography. Acta Crystallogr. D Biol. Crystallogr. *66*, 12–21. https://doi.org/10.1107/S0907444909042073.

101. Barad, B.A., Echols, N., Wang, R.Y.R., Cheng, Y., Dimaio, F., Adams, P. D., and Fraser, J.S. (2015). EMRinger: Side chain-directed model and map validation for 3D cryo-electron microscopy. Nat. Methods *12*, 943–946. https://doi.org/10.1038/nmeth.3541.

102. Schrödinger, L., and DeLano, W. (2020). The PyMOL Molecular Graphics System, [Version 3.0]. https://www.pymol.org/support.html?

103. Racine, J.S. (2012). Rstudio: A Platform-Independent Ide for R and Sweave. J. Appl. Econ. *27*, 167–172. https://doi.org/10.1002/jae.1278.

104. Gaidatzis, D., Lerch, A., Hahne, F., and Stadler, M.B. (2015). QuasR: quantification and annotation of short reads in R. Bioinformatics *31*, 1130–1132. https://doi.org/10.1093/bioinformatics/btu781.

105. Langmead, B., Trapnell, C., Pop, M., and Salzberg, S.L. (2009). Ultrafast and memory-efficient alignment of short DNA sequences to the human genome. Genome Biol. *10*, R25. https://doi.org/10.1186/gb-2009-10-3-r25.

106. Zhang, Y., Liu, T., Meyer, C.A., Eeckhoute, J., Johnson, D.S., Bernstein, B.E., Nusbaum, C., Myers, R.M., Brown, M., Li, W., et al. (2008). Model-based analysis of ChIP-Seq (MACS). Genome Biol. *9*, R137. https://doi.org/10.1186/gb-2008-9-9-r137.

107. Gu, Z., Eils, R., Schlesner, M., and Ishaque, N. (2018). EnrichedHeatmap: an R/Bioconductor package for comprehensive visualization of genomic signal associations. BMC Genomics *19*, 234. https://doi.org/10.1186/s12864-018-4625-x.

108. Mohn, F., Weber, M., Rebhan, M., Roloff, T.C., Richter, J., Stadler, M.B., Bibel, M., and Schübeler, D. (2008). Lineage-specific polycomb targets and de novo DNA methylation define restriction and potential of neuronal progenitors. Mol. Cell *30*, 755–766. https://doi.org/10.1016/j.molcel.2008.05.007.

109. Abdulrahman, W., Uhring, M., Kolb-Cheynel, I., Garnier, J.-M., Moras, D., Rochel, N., Busso, D., and Poterszman, A. (2009). A set of baculovirus transfer vectors for screening of affinity tags and parallel expression strategies. Anal. Biochem. *385*, 383–385. https://doi.org/10.1016/j.ab.2008.10.044.

110. Jolma, A., Yan, J., Whitington, T., Toivonen, J., Nitta, K.R., Rastas, P., Morgunova, E., Enge, M., Taipale, M., Wei, G., et al. (2013). DNA-binding specificities of human transcription factors. Cell *152*, 327–339. https://doi.org/10.1016/j.cell.2012.12.009.

111. Iurlaro, M., Masoni, F., Flyamer, I.M., Wirbelauer, C., Iskar, M., Burger, L., Giorgetti, L., and Schübeler, D. (2024). Systematic assessment of ISWI subunits shows that NURF creates local accessibility for CTCF. Nat. Genet. *56*, 1203–1212. https://doi.org/10.1038/s41588-024-01767-x.

112. Lienert, F., Wirbelauer, C., Som, I., Dean, A., Mohn, F., and Schübeler, D. (2011). Identification of genetic elements that autonomously determine DNA methylation states. Nat. Genet. *43*, 1091–1097. https://doi.org/10.1038/ng.946.

113. Rosenthal, P.B., and Henderson, R. (2003). Optimal Determination of Particle Orientation, Absolute Hand, and Contrast Loss in Single-particle Electron Cryomicroscopy. J. Mol. Biol. *333*, 721–745. https://doi.org/10.1016/j.jmb.2003.07.013.

114. Chen, S., McMullan, G., Faruqi, A.R., Murshudov, G.N., Short, J.M., Scheres, S.H.W., and Henderson, R. (2013). High-resolution noise substitution to measure overfitting and validate resolution in 3D structure determination by single particle electron cryomicroscopy. Ultramicroscopy *135*, 24–35. https://doi.org/10.1016/j.ultramic.2013.06.004.

115. de la Rosa-Trevín, J.M., Otón, J., Marabini, R., Zaldívar, A., Vargas, J., Carazo, J.M., and Sorzano, C.O.S. (2013). Xmipp 3.0: An improved software suite for image processing in electron microscopy. J. Struct. Biol. *184*, 321–328. https://doi.org/10.1016/j.jsb.2013.09.015.

116. Quinlan, A.R., and Hall, I.M. (2010). BEDTools: a flexible suite of utilities for comparing genomic features. Bioinformatics *26*, 841–842. https://doi.org/10.1093/bioinformatics/btq033.

117. Pagès, H., Aboyoun, P., Gentleman, R., DebRoy, S., Carey, V., Delhomme, N., Ernst, F., Huber, W., Khan, H., Lakshman, A., et al. (2025). Biostrings: efficient manipulation of biological strings. R package version 2.76.0. Bioconductor. https://bioconductor.org/packages/Biostrings.

118. R Core Team (2022). R: A Language and Environment for Statistical Computing. In R Foundation for Statistical Computing https://cran.r-project.org/doc/manuals/r-release/fullrefman.pdf.

119. Lawrence, M., Huber, W., Pagès, H., Aboyoun, P., Carlson, M., Gentleman, R., Morgan, M.T., and Carey, V.J. (2013). Software for computing and annotating genomic ranges. PLoS Comput. Biol. *9*, e1003118. https://doi.org/10.1371/journal.pcbi.1003118.

120. Villanueva, R.A.M., and Chen, Z.J. (2019). ggplot2: Elegant Graphics for Data Analysis (2nd ed.). Meas.: Interdiscip. Res. Perspect. *17*, 160–167. https://doi.org/10.1080/15366367.2019.1565254.

121. Eng, J.K., McCormack, A.L., and Yates, J.R. (1994). An approach to correlate tandem mass spectral data of peptides with amino acid sequences in a protein database. J. Am. Soc. Mass Spectrom. *5*, 976–989. https://doi.org/10.1016/1044-0305(94)80016-2.

122. Cox, J., and Mann, M. (2008). MaxQuant enables high peptide identification rates, individualized p.p.b.-range mass accuracies and proteome-wide protein quantification. Nat. Biotechnol. *26*, 1367–1372. https://doi.org/10.1038/nbt.1511.

123. Elias, J.E., and Gygi, S.P. (2007). Target-decoy search strategy for increased confidence in large-scale protein identifications by mass spectrometry. Nat. Methods *4*, 207–214. https://doi.org/10.1038/nmeth1019.

124. Combe, C.W., Fischer, L., and Rappsilber, J. (2015). xiNET: cross-link network maps with residue resolution. Mol. Cell. Proteomics *14*, 1137–1147. https://doi.org/10.1074/mcp.O114.042259.

125. Lagerwaard, I.M., Albanese, P., Jankevics, A., and Scheltema, R.A. (2022). Xlink Mapping and AnalySis (XMAS) - Smooth Integrative Modeling in ChimeraX. Preprint at bioRxiv. https://doi.org/10.1101/2022.04.21.489026.

126. Kahraman, A., Malmström, L., and Aebersold, R. (2011). Xwalk: computing and visualizing distances in cross-linking experiments. Bioinformatics *27*, 2163–2164. https://doi.org/10.1093/bioinformatics/btr348.

127. Perez-Riverol, Y., Bai, J., Bandla, C., García-Seisdedos, D., Hewapathirana, S., Kamatchinathan, S., Kundu, D.J., Prakash, A., Frericks-Zipper, A.,

Eisenacher, M., et al. (2022). The PRIDE database resources in 2022: a hub for mass spectrometry-based proteomics evidences. Nucleic Acids Res. *50*, D543–D552. https://doi.org/10.1093/nar/gkab1038.

128. Langmead, B., Schatz, M.C., Lin, J., Pop, M., and Salzberg, S.L. (2009). Searching for SNPs with cloud computing. Genome Biol. *10*, R134. https://doi.org/10.1186/gb-2009-10-11-r134.
129. Amemiya, H.M., Kundaje, A., and Boyle, A.P. (2019). The ENCODE Blacklist: Identification of Problematic Regions of the Genome. Sci. Rep. *9*, 9354. https://doi.org/10.1038/s41598-019-45839-z.
130. Ross-Innes, C.S., Stark, R., Teschendorff, A.E., Holmes, K.A., Ali, H.R., Dunning, M.J., Brown, G.D., Gojis, O., Ellis, I.O., Green, A.R., et al. (2012). Differential oestrogen receptor binding is associated with clinical outcome in breast cancer. Nature *481*, 389–393. https://doi.org/10.1038/nature10730.
131. Stark, R., and Brown, G. (2025). DiffBind: Differential Binding Analysis of ChIP-Seq Peak Data. Bioconductor. https://bioconductor.org/packages/devel/bioc/vignettes/DiffBind/inst/doc/DiffBind.pdf.
132. Kundaje, A., Boley, N., Bickel, P.J., and Lee, J. (2014). ENCODE: TF ChIP-seq peak calling using the irreproducibility discovery rate (IDR) framework. GitHub. https://github. com/kundajelab/idr.
133. Li, Q., Brown, J.B., Huang, H., and Bickel, P.J. (2011). Measuring reproducibility of high-throughput experiments. Ann. Appl. Stat. *5*, 1752–1779. https://doi.org/10.1214/11-AOAS466.
134. Gu, Z., Gu, L., Eils, R., Schlesner, M., and Brors, B. (2014). circlize Implements and enhances circular visualization in R. Bioinformatics *30*, 2811–2812. https://doi.org/10.1093/bioinformatics/btu393.

STAR★METHODS

KEY RESOURCES TABLE

REAGENT or RESOURCE	SOURCE	IDENTIFIER
Antibodies		
p53 (1C12) Mouse mAb	Cell Signaling Technology	Cat# 2524S
Anti-USP7	Thermo Fisher Scientific	Cat# A300-033A
V5-tag monoclonal	Thermo Fisher Scientific	Cat# R960-25
Anti-IgG	Sigma-Aldrich	Cat# M7023
Bacterial and virus strains		
E. coli BL21-CodonPlus(DE3)-RIL	Agilent	Cat# 230245
NEB Stable Competent *E. coli*	NEB	Cat# C3040H
Chemicals, peptides, and recombinant proteins		
Protease inhibitor cocktail	Sigma (Merck)	Cat# S8830
Doxorubicin	Sigma-Aldrich	Cat# 44583
Ub-Rh110Gly (UbiQ-002)	UbiQ, the Netherlands	Cat# UbiQ-002
K48-Tetra-Ubiquitin Fluorescein-Labeled	LifeSensors	Cat# SI4804F
K63-Linked Tetra-Ubiquitin, TAMRA-labeled	LifeSensors	Cat# SI6304T
Phusion™ High-Fidelity DNA Polymerases (2 U/μL)	Thermo Fisher Scientific	Cat# F530L
Phusion™ HF Buffer Pack	Thermo Fisher Scientific	Cat# F518L
dNTP Mix (10 mM each)	Thermo Fisher Scientific	Cat# R0192
Cellfectin™ II	Thermo Fisher Scientific	Cat# 10362100
Desthiobiotin	IBA	Cat# 2-1000-005
QIAquick Gel Extraction kit	Qiagen	Cat# 28706
SYBR GOLD Nucleic acid stain	Invitrogen	Cat# S11494
NEBNext Ultra DNA library prep kit for Illumina	NEB	Cat# E7370L
NEBNext Multiplex Oligos for Illumina (Dual index primers set 1)	NEB	Cat# E7600S
CUTANA pAG-MNase	Epicypher	Cat# 15-1016
MinElute PCR Purification Kit	Qiagen	Cat# 28004
DSSO	Thermo Fisher Scientific	Cat# A33545
Deposited data		
p53-NCP$^{SHL-5.7}$ non-XL model	This study	PDB: 9R2Q
p53-NCP$^{SHL-5.7}$ non-XL map	This study	EMD-53537
p53-NCP$^{SHL-5.7}$ XL model	This study	PDB: 9R04
p53-NCP$^{SHL-5.7}$ XL map	This study	EMD-53478
p53-NCP$^{SHL+5.9}$ XL model	This study	PDB: 9R2P
p53-NCP$^{SHL+5.9}$ XL map	This study	EMD-53536
p53-NCP$^{SHL+5.9}$ non-XL model	This study	PDB: 9R2M
p53-NCP$^{SHL+5.9}$ non-XL map (full map)	This study	EMD-53534
p53-NCP$^{SHL+5.9}$ non-XL map (focus refined map of p53)	This study	EMD-53535
p53-NCP$^{SHL+5.9}$ non-XL map (composite map)	This study	EMD-53532
USP7^{FL}-p53-NCP$^{SHL-5.7}$ map	This study	EMD-53517
USP7^{FL}-p53-NCP$^{SHL-5.7}$ model	This study	PDB-IHM: 9A9W
Monomeric E6AP-E6-p53 ternary complex map	This study	EMD-18809
Monomeric E6AP-E6-p53 ternary complex model	This study	PDB: 8R1F
Dimeric E6AP-E6-p53 ternary complex map	This study	EMD-18810
Dimeric E6AP-E6-p53 ternary complex model	This study	PDB: 8R1G

(*Continued on next page*)

Continued

REAGENT or RESOURCE	SOURCE	IDENTIFIER
XL-MS (p53-NCP SHL-5.7)	This study	PXD054140
XL-MS (p53-USP7-NCP SHL-5.7)	This study	PXD054141
TET models (Zenodo)	This study	10.5281/zenodo.15268030
ChIPseq_ESC_wt_p53_Unt	Isbel et al.[15]	GEO: GSM6038035, GSM6038036
ChIPseq_ESC_wt_p53_Act	Isbel et al.[15]	GEO: GSM6038037, GSM6038038
ChIPseq_ESC_wt_IgG_Unt	Isbel et al.[15]	GEO: GSM6038043, GSM6038044
ChIP-seq	This study	GEO: GSE299056
Cut & Run	This study	GEO: GSE299057
p53-nucleosomes clash analysis code (Zenodo)	This study	https://doi.org/10.5281/zenodo.15706014
Experimental models: Cell lines		
Wildtype mouse embryonic stem cells, a TC-1 line, background 129S6/SvEvTac.	Line was originally obtained from A. Dean at the National Institutes of Health. Lienert et al.[91]	Mouse embryonic stem cells: EY wildtype mESCs
p53 v5-taged mouse embryonic stem cells, a TC-1 line, background 129S6/SvEvTac.	Isbel et al.[15]	Mouse embryonic stem cells: p53.V5.dTag mESCs
GFP-expressing mouse embryonic stem cells, a TC-1 line, background 129S6/SvEvTac.	Isbel et al.[15]	Mouse embryonic stem cells: Cag.eGFP mESCs
Experimental models: Organisms/strains		
E. coli BL21-CodonPlus(DE3)-RIL	Agilent	Cat# 230245
Sf9 Insect cells	Thermo Fisher	Cat#11496015
High-Five Insect cells	Thermo Fisher	Cat# B85502
Oligonucleotides		
p53 library DNA sequence	TWIST Biosciences	N/A
Fluorescein-p53 oligo (CGGACATGCCCG GGCATGTCCG)	Microsynth	N/A
Cy5-p53-oligo (Cy5AGGACTAAC ATGCCCGGGCATGTCTAAGCT)	Microsynth	N/A
Atto-p53 (ATCCTGGAGAAACATG CCCGGGCATGTCCTCAATTGGTCGTA)	Microsynth	N/A
Recombinant DNA		
pAC8-Strep-TEV-p53	This study	N/A
pAC8-Strep-TEV-p53-DBD	This study	N/A
pAC8-Strep-TEV-USP7	This study	N/A
pET-28a-His-TEV-TRAF	This study	N/A
pAC8-Strep-TEV-E6AP	This study	N/A
pET-28a-His-SUMO-E6 (C80S, C97S, C111S, C140S)	This study	N/A
Software and algorithms		
FEI EPU v2.7.0	Thermo Scientific	https://www.thermofisher.com/
cryoFLARE	Schenk et al.[92]	https://www.cryoflare.org/
Relion 3	Zivanov et al.[93]	https://github.com/3dem/relion
cryoSPARC v3-v4	Punjani et al.[94]	https://cryosparc.com/
ChimeraX	Pettersen et al.[95]	https://www.rbvi.ucsf.edu/chimerax/
Coot	Emsley and Cowtan[96]	https://www2.mrc-lmb.cam.ac.uk/personal/pemsley/coot/
ISOLDE v1.3	Croll[97]	https://isolde.cimr.cam.ac.uk/
AlphaFold v2.3	Jumper et al.[98]	https://github.com/deepmind/alphafold

(*Continued on next page*)

Continued

REAGENT or RESOURCE	SOURCE	IDENTIFIER
PHENIX	Adams et al.[99]	https://phenix-online.org/
Molprobity	Chen et al.[100]	https://github.com/rlabduke/MolProbity
EMRinger	Barad et al.[101]	https://github.com/fraser-lab/EMRinger
PyMol v2.3.3	Schrodinger, LLC, 2020125[102]	https://pymol.org/2/
Proteome Discoverer v.2.5	Thermo Fisher Scientific	Cat# OPTON-31014
R studio 4.4.0 or higher	Racine[103]	https://www.r-project.org
Bioconductor QuasR	Gaidatzis et al.[104]	https://doi.org/10.18129/B9.bioc.QuasR
Bowtie	Langmead et al.[105]	https://bowtie-bio.sourceforge.net/index.shtml
MACS2	Zhang et al.[106]	https://pypi.org/project/MACS2/
Bioconductor EnrichedHeatmap	Gu et al.[107]	https://www.bioconductor.org/packages/release/bioc/html/EnrichedHeatmap.html
Other		
SF4 Baculo-Express Media	BioConcept	Cat# 900F38
HiLoad Superdex™ 200 pg preparative SEC column	Cytiva	Cat# 28989335
HiTrap™ Q HP	Cytiva	Cat# 17115301
Amicon Ultra-4 Centrifugal Filter Unit, Ultracel-50 30 Kda, 4mL	Merck (EMD Millipore)	Cat# UFC803096
Amicon Ultra-15 Centrifugal Filter Unit, Ultracel, 30 Kda, 15 mL	Merck (EMD Millipore)	Cat# UFC903024
Mono Q 5/50 GL	Cytiva	Cat# 17-5166-01
Strep-Tactin Sepharose 50% suspension	IBA	Cat# 2-1201-010-BULK5
POROS Heparin	Thermo Fisher	Cat# 4329435
Superdex 200 10/300	Cytiva	Cat# 17517501
POROS HQ	Thermo Fisher	Cat# 82077
Superose 6 10/300 Increase	Cytiva	Cat# 29091596
HisTrap HP, 5 ml	Cytiva	Cat# 17-5248-02
Superose 6 Increase 3.2/300	Cytiva	Cat# 29091598
QIAquick Gel Extraction spin columns	Qiagen	Cat# 28115
concanavalin A magnetic beads	Bangs Laboratories	Cat# BP531
AMPure XP beads	Beckman Coulter	Cat# A63881

EXPERIMENTAL MODEL AND STUDY PARTICIPANT DETAILS

Mouse ES cells were cultured as described previously.[108] Briefly, cells were maintained in Dulbecco's modified Eagle medium (DMEM, Invitrogen), supplemented with 15% fetal calf serum (Invitrogen), l-glutamine (Gibco) and nonessential amino acids (Gibco), betamercaptoethanol (Sigma) and leukemia inhibitory factor (produced in-house). Experiments were performed with cells grown for several passages on plates coated with 0.2% gelatin (Sigma).

METHOD DETAILS

Expression, purification and reconstitution of histone octamers

Human histones H2A, H2B, H3 and H4 were expressed and purified from *Escherichia coli* using an N-terminal His_6-tag. Cells were lysed by sonication in a buffer A containing 50 mM Tris pH 8.0, 500 mM NaCl, 1 mM PMSF and 5% glycerol. Following centrifugation (27,216 x g, for 20 minutes) the insoluble portion was resuspended in buffer A containing 7 M guanidine hydrochloride, followed by an additional round of centrifugation (27,216 x g, for 20 minutes). Filtered supernatant was then loaded onto a HiTrap His column (Cytiva) and washed with buffer B (50 mM Tris pH 8.0, 500 mM NaCl, 6 M urea, 5 mM imidazole and 5% glycerol) until absorbance is low. The histones were eluted with a linear gradient of 5-500 mM imidazole in buffer B. The eluted fractions were then dialyzed against a buffer containing 5 mM Tris pH 7.5, and 1 mM DTT. Thrombin protease treatment (1 unit/mg of histones, GE Healthcare) at room temperature for 3 hours was used to remove the His_6 tags. After thrombin cleavage, each histone was then subjected to Poros Q column (Thermo Fisher) chromatography. The column was washed with 20 mM sodium acetate pH 5.2, 200 mM NaCl, 1 mM DTT, 1 mM EDTA and 6 M urea, and then eluted with a linear gradient of NaCl from 200 to 900 mM. Upon lyophilization, the purified histones

were mixed in a denaturing buffer containing 20 mM Tris-HCl pH 7.5, 6 M guanidine hydrochloride and 1 mM DTT. Samples were dialyzed against refolding buffer containing 20 mM Tris-HCl pH 7.5, 2 M KCl and 1 mM DTT. Further, the histone complexes were purified by size-exclusion chromatography (HiLoad Superdex™ 200 pg; Cytiva).

DNA purification and reconstitution of nucleosome

Large scale generation of DNA was performed using Phusion (Thermo Fischer Scientific) PCR amplification. The resulting amplified DNA was purified by a HiTrap Q HP column (Cytiva). The purified DNA was dialysed overnight in 20 mM Tris-HCl pH 7.5, and further concentrated using 30 kDa concentrator (Amicon Ultra, Merck Millipore) and stored at -20°C until usage.

Large scale nucleosome reconstitution for cryo-EM

The purified DNA and the histone octamer complex were reconstituted at a 1:1.5 molar ratio in presence of 2 M KCl. The complex was dialyzed against refolding buffer (RB) 'high' (10 mM Tris-HCl pH 7.5, 2 M KCl, 1 mM EDTA and 1 mM DTT). Upon slow dialysis, there was gradual reduction in the concentration of KCl from 2 M to 0.25 M using a peristaltic pump with RB 'low' buffer (10 mM Tris-HCl pH 7.5, 250 mM KCl, 1 mM EDTA and 1 mM DTT) at 4°C. The reconstituted nucleosomes were incubated at 55°C for 1.5 h, and further purified using a MonoQ 5/50 ion-exchange gradient (Cytiva) and dialyzed into 20 mM Tris-HCl pH 7.5 and 500 μM TCEP overnight. The nucleosomes were concentrated using 30 kDa concentrators (Amicon Ultra, Merck Millipore) and stored at 4°C.

Small scale nucleosome reconstitution for deubiquitination assays, EMSA and FIDA

The purified DNA (~300 pmoles) and the histone octamer complex were set-up in multiple smaller scales in buffer 'high' containing 30 mM Tris-HCl pH 7.5, 4 M KCl and 1 mM DTT, and incubated at 37°C for 20 min. Subsequently, buffer 'low' containing 20 mM Tris-HCl pH 7.5 and 1 mM DTT was added every 20 min for 1h 20 min with a final incubation at 55°C for 1 h. After the dialysis, the nucleosomes were purified using a MonoQ 5/50 ion-exchange gradient (Cytiva) and dialyzed into 20 mM Tris-HCl pH 7.5 and 500 μM TCEP overnight. The nucleosomes were concentrated using 30 kDa concentrators (Amicon Ultra, Merck Millipore) and stored at 4°C.

Protein expression and purification

p53

Human full-length p53 (residues 1-393) was cloned into pAC-derived vector containing an N-terminal Strep II tag.[109] The protein was expressed from 4 L of *Trichoplusia ni* High Five (Hi5) cells using the Bac-to-Bac system (Thermo Fisher Scientific). The cells were cultured at 27°C and harvested two days after infection with the baculovirus. The cells were resuspended in lysis buffer (20 mM Tris-HCl pH 8.0, 1 M sodium chloride, 0.5 mM TCEP, 10% glycerol and 1 tablet protease inhibitor cocktail (Merck) and lysed by sonication. The lysate was centrifuged at 40k rpm using a Type 45 Ti Fixed-Angle rotor (Beckman Coulter) for 45 min at 4°C and the supernatant was filtered and loaded onto a gravity column containing a Strep-Tactin Sepharose bead slurry (IBA life sciences) for affinity chromatography. The protein was eluted in buffer containing 150 mM sodium chloride and 5 mM desthiobiotin. The protein was subjected to further purification by using heparin column (Thermo Fisher) and eluted with a linear gradient using 1M sodium chloride as buffer B. Further, the protein was purified by size-exclusion chromatography (Superdex 200; Cytiva) in buffer containing 20 mM HEPES pH 8.0, 150 mM sodium chloride, 5% glycerol, 0.5 mM TCEP. The purified proteins were concentrated using 30 kDa concentrators (Amicon Ultra, Merck Millipore) and stored at -80°C. The DBD (residues 92-292) was also subcloned into a pAC-vector containing an N-terminal Strep II tag and expressed in 4 L of *Spodoptera frugiperda* (Sf9) cells (Thermo Fisher Scientific). The protein was purified by Strep-Tactin affinity chromatography (IBA life sciences) and eluted with 2.5 mM desthiobiotin in buffer containing 150 mM sodium chloride. The protein was further subjected to heparin ion-exchange and size-exclusion chromatography (Superdex 200; Cytiva) and eluted in buffer containing 20 mM HEPES pH 7.5, 150 mM sodium chloride, 5% glycerol, 0.5 mM TCEP.

USP7

Human full-length USP7 (residues 1-1102) was cloned into pAC-derived vector containing an N-terminal Strep II tag.[109] USP7 was expressed from *Trichoplusia ni* High Five (Hi5) cells using the Bac-to-Bac system (Thermo Fisher Scientific). Upon infection with the baculovirus, the cells were harvested after two days, resuspended in lysis buffer (20 mM HEPES pH 7.5, 1 M sodium chloride, 1 mM EDTA pH 7.5, 0.5 mM TCEP, 5% glycerol and 1 tablet protease inhibitor cocktail (Merck) and lysed by sonication. Following purification by affinity chromatography, the protein was eluted with 2.5 mM desthiobiotin in a buffer containing 150 mM sodium chloride. The Strep (II) eluted fractions were diluted to 100 mM sodium chloride and loaded on POROS HQ column and eluted with a linear gradient using 1 M sodium chloride. The purified proteins were purified by size-exclusion chromatography (Superose 6; Cytiva) in a buffer containing 20 mM HEPES pH 7.5, 100 mM sodium chloride, 5% glycerol, 0.5 mM TCEP. Pure fractions were collected, concentrated and stored at -80°C.

The TRAF domain (residues 1-208) of USP7 was subcloned into a pET28-derived vector containing an N-terminal 6x His tag for expression in *Escherichia coli*. Cells were grown aerobically at 37°C in 4 L LB medium with Kanamycin. At an optical density ($OD_{600\ nm}$) of 0.6-0.8, the cultures were induced with 0.2 mM IPTG (final concentration), grown at 18°C, 200 rpm overnight. The cells were centrifuged at 4°C for 15 minutes and the pellet was stored overnight in -20°C. Upon resuspension of the cells in lysis buffer/His buffer A (50 mM Tris-HCl pH 6.8, 400 mM sodium chloride, 20 mM Imidazole, 0.5 mM TCEP, 5% glycerol, 1 tablet protease inhibitor cocktail (Sigma)), the cells were disrupted by sonication, and further centrifuged at 40k rpm using a Type 45 Ti Fixed-Angle rotor (Beckman Coulter) for 40 minutes at 4°C. The supernatant was subjected to a HisTrap HP column (5 mL, Cytiva), washed with buffer

(50 mM Tris-HCl pH 6.8, 1 M sodium chloride, 20 mM Imidazole, 0.5 mM TCEP, 5% glycerol) and purified in His buffer B (50 mM Tris-HCl pH 6.8, 400 mM sodium chloride, 500 mM imidazole, 0.5 mM TCEP, 5% glycerol). The relevant fractions were pooled, TEV-cleaved at 4°C and loaded on POROS HQ column and eluted with a linear gradient using 1 M sodium chloride. Further, following purification by SEC (Superdex 200, Cytiva), the proteins were eluted in 50 mM Tris-HCl pH 6.8, 150 mM sodium chloride, 0.5 mM TCEP and 5% glycerol, concentrated and stored in -80°C.

E6AP

Human full-length E6AP (residues 1-875) with an N-terminal Strep (II) tag was expressed in *Trichoplusia ni* High Five insect cells following similar methods as described before. The cells were harvested and lysed by sonication in buffer containing 25 mM Tris pH 8.0, 200 mM sodium chloride, 5% glycerol, 0.5 mM TCEP, 5 mM magnesium chloride, 1 tablet protease inhibitor cocktail (Roche Applied Science) and 0.1% Triton X-100. Using Strep-Tactin Sepharose bead slurry (IBA life sciences) for affinity chromatography, a low salt (200 mM sodium chloride) buffer was used to wash the column, followed by high salt (1M sodium chloride), and the protein was eluted at 200 mM sodium chloride and 5 mM desthiobiotin. The eluted fractions were diluted to 100 mM sodium chloride, prior to application on a POROS-HQ μm column (Life Technologies) and further eluted with a linear gradient using 2 M sodium chloride as Buffer B. The sample was then subjected to SEC (Superose 6, Cytiva) in a buffer containing 25 mM Tris pH 8.0, 150 mM sodium chloride, 5% glycerol, 0.5 mM TCEP. Pure fractions were concentrated and stored at -80°C.

E6

Full-length HPV16 E6 (residues 1-158) containing four amino acid substitutions (C80S, C97S, C111S, C140S) was cloned into a pET-28(+) vector with an N-terminal 6xHis and SUMO tag for *Escherichia coli* expression. 4-6 L of culture was inoculated in a 1:100 (v/v) ratio with an overnight pre-culture and incubated at 37°C with Kanamycin. Upon reaching an $OD_{600\ nm}$ of 0.6-1.0, gene expression was induced with 0.5 mM IPTG induction. Cells were harvested by centrifugation at 4°C for 10 min and resuspended in 100-200 mL lysis buffer containing 50 mM Tris pH 6.8, 400 mM sodium chloride, 20 mM Imidazole, 5% glycerol and 0.5 mM TCEP. The resuspended pellet was sonicated prior to lysate clarification through ultracentrifugation at 40k rpm using a Type 45 Ti Fixed-Angle rotor (Beckman Coulter) for 1 hour. Filtered supernatant was loaded onto a HiTrap His column (Cytiva). After loading, the column was washed with wash buffer until absorbance is low and eluted with 10-80% gradient in buffer containing 50 mM Tris pH 6.8, 400 mM sodium chloride, 500 mM imidazole, 5% glycerol and 0.5 mM TCEP. The eluted fractions were then further purified with a heparin column by first diluting to <200 mM sodium chloride before loading and using a linear sodium chloride salt gradient. Finally, samples were diluted/dialyzed to no less than 400 mM salt and flash frozen in 5-10% glycerol and stored at -80°C.

SeEN-seq library preparation

The HT-SELEX derived p53 motif[110] (AACATGCCCGGGCATGTC, JASPAR Matrix ID: MA0106.3) was tiled through the Widom 601 (W601) sequence at 1 bp intervals across the entire 147 bp nucleosome positioning sequence, resulting in a library of 130 DNA sequences with different motif positions. The p53 library DNA sequences were flanked by EcoRV sites and adapter sequences and were ordered as gene fragments from TWIST Biosciences. Individual gene fragments were suspended, equimolar amounts were pooled and cut with EcoRV-HF (NEB). The resulting 153bp DNA fragments were purified from a 3% agarose gel using the QIAquick Gel Extraction kit (Qiagen). p53 motif containing DNA fragments were mixed with an excess of W601 DNA (1:30 molar ratio) for nucleosome assembly.

Generation of linker SeENseq pool

SeEN-seq nucleosomes were assembled and purified following the protocol described above, where the 601 p53 motif library DNA pool was PCR amplified with primers that extended the 5' flanking DNA by 20bp and spiked with distinct amplicons representing the p53 motif tiled throughout the 5' flanking 601 DNA at approximately equimolar concentration relative to the individual library tiles. The resulting pool represented an extended 170 bp 601 sequence with the HT-SELEX derived p53 motif[110] (AACATGCCCGGGCATGTC, JASPAR Matrix ID: MA0106.3) tiled at every possible position throughout the 20 bp 5' flanking and nucleosomal W601 sequence, up to final 23bp of the 601 sequence where it was necessary to design a 3' primer to generate the amplicons.

SeEN-seq assay

SeEN-seq was performed as before[9] with some modifications. Nucleosomes (100 nM) were incubated for 1 hour at room temperature with full-length p53 (250 nM) in 20 μL reactions containing 20 mM Tris-HCl pH 7.5, 75 mM sodium chloride, 10 mM potassium chloride, 1 mM magnesium chloride, 0.1 mg/mL BSA, and 1 mM DTT. For each condition, 3 technical replicates were generated. Reactions were loaded onto 6% non-denaturing polyacrylamide gels (acrylamide:bis-acrylamide = 37.5:1) in 0.5x TGE and run for 1.2 h (150V, room temperature). Gels were stained with SYBR gold nucleic acid stain (10 min, Invitrogen) and DNA bands corresponding to p53-bound and unbound nucleosome complexes were excised. EMSA gel slices were incubated with 100 μL acrylamide gel extraction buffer (500 mM ammonium acetate, 10 mM magnesium acetate, 1 mM EDTA, 0.1% SDS) for 30 min at 50°C. A pre-mix of water (50 μL per sample) and QIAquick Gel Extraction kit QG buffer (450 μL per sample) was added, and samples were incubated for an additional 30 min at 50°C. After a short spin, the supernatant was transferred to QIAquick Gel Extraction spin columns and DNA fragments were purified according to the manufacturer's instructions. DNA was eluted in water (22 μL) and approximately half of the sample (10 μL, 1-10 ng DNA) was used for NGS library preparation (NEBNext Ultra DNA library prep kit for Illumina, E7370S/L, NEB) with dual indexing (E7600S, NEB) and 12 cycles of PCR amplification. Purified sequencing libraries were quantified by Qubit (Thermo

Fisher), equimolar amounts were pooled, and the library size was checked using the HS DNA assay on an Agilent 2100 Bioanalyzer instrument. Finally, samples were sequenced on an Illumina NextSeq platform (300 bp paired-end).

CUT & RUN

Cleavage under targets and release using nuclease assays (CUT & RUN) were performed as previously described[111] and based on the EpiCypher manufacturer's protocol (v.1.5) with some modifications. Approximately 24 h before the experiment, mouse stem cells with the V5 tag integrated into the 5' end of the p53 gene[15,112] were seeded into 6-well dishes ($\sim 5 \times 10^5$ cells/well) and where applicable, the media was exchanged with fresh media and containing 1 μM doxorubicin (#44583, Sigma-Aldrich) for four hours prior to harvesting. In brief, 10 μL per sample of concanavalin A beads (concanavalin A magnetic beads; Bangs Laboratories, BP531) were washed twice with bead activation buffer (20 mM HEPES pH 7.9, 10 mM KCl, 1 mM calcium chloride and 1 mM manganese(II) chloride and resuspended in 10 μL of the bead activation buffer. For each sample, 5×10^5 cells were washed in PBS and centrifuged at room temperature at 600g for 3 min. Cells were then washed twice in 100 μL of wash buffer (20 mM HEPES pH 7.5, 150 mM sodium chloride, 0.5 mM spermidine, 1 tablet protease inhibitor-Roche) and resuspended in 100 μL of the same wash buffer. Afterward, cells were aliquoted in eight-well strip tubes containing 10 μL of activated beads, mixed with gentle vortexing and incubated at room temperature for 10 min. After this time, supernatant was removed, and beads were gently resuspended in 50 μL of cold antibody buffer (wash buffer + 0.001% digitonin + 2 mM EDTA). At this point, 0.5 μL of antibody (V5 tag, R960-25, Thermo Fisher Scientific) were added to each sample and left overnight at 4 °C. The following day, beads were washed twice using 250 μL of cold digitonin buffer (wash buffer + 0.001% digitonin) and gently resuspended in 50 μL of the same buffer. At this point, 2.5 μL of CUTANA pAG-MNase (20x pAG-MNase; Epicypher, 15-1016) were added to each of the samples, which were then gently mixed and left for 10 min at room temperature. After this time, 250 μL of cold digitonin buffer was added directly to the samples. The previous step was repeated for two washes, and then samples were resuspended in 50 μL of digitonin buffer. To start the MNase reaction, 2 μL of 50 mM calcium chloride was added to the samples, which were then gently mixed and left at 4 °C for 2 h. After this time, 33 μL of stop buffer (340 mM sodium chloride, 20 mM EDTA, 4 mM EGTA, 50 μg mL^{-1} RNase A and 50 μg mL^{-1} glycogen) were added, and samples were then vortexed and incubated at 37 °C for 10 min. Samples were moved on the magnet, and the supernatant was transferred to clean 1.5 mL tubes for nucleic acid extraction using the MinElute PCR Purification Kit (Qiagen). Purified DNA was used for library preparation using the NEBNext Ultra Library Prep Kit (Illumina) according to the manufacturer's instructions with the following Epicypher manufacturer's modifications. DNA clean-up before PCR amplification was done using 1.1x AMPure XP beads. PCR amplification parameters were adjusted to 1 cycle of 45 s at 98 °C, 14 cycles of 15 s at 98 °C followed by 10 s at 60 °C and 1 cycle of 1 min at 72 °C. DNA was again purified using 1.1× AMPure XP beads and eluted in 0.1x TE buffer. Libraries were analyzed and quantified using Agilent Bioanalyzer and sequenced on the Illumina NextSeq platform at 41 bp paired-end.

Generation of double-stranded oligonucleotides

Double-stranded oligo corresponding to the p53 motif was generated by performing an annealing reaction using unlabeled and fluorescein labeled oligo (CGGACATGCCCGGGCATGTCCG) in 10x annealing buffer (100 mM Tris-HCl pH 7.5, 500 mM sodium chloride, 10 mM EDTA pH 7.4) for 75 cycles in the thermal cycler.

Size-exclusion chromatography (SEC)

The complex formation was analyzed by SEC runs on Superose 6 Increase 3.2/300 (Cytiva) analytical column at 900 pmoles (~60-80 μL, 1:4.5 molar ratio of nucleosome to proteins) in 20 mM HEPES pH 8.0, 150 mM sodium chloride, 5% glycerol, 0.5 mM TCEP. Proteins were incubated for ~30 min before injection into the column. The content of each peak was evaluated by SDS/PAGE and Coomassie staining.

SEC-MALS

Forty microliters of sample were injected onto a Superose 6 Increase 10/300 GL column (Cytiva) using an Agilent Infinity 1260 II HPLC system. In-line refractive index and light scattering measurements were performed using a Wyatt Optilab T-rEX refractive index detector and a Wyatt miniDAWN TREOS 3 light scattering detector. System control and analysis was carried out using the Wyatt Astra 7.3.1 software. System performance was checked with BSA (initial and final run).

Mass photometry

Protein dilutions were made in MP buffer (20 mM Tris-HCl pH 8.0, 100 mM potassium chloride and 0.5 mM TCEP) and mixed in a 1:1:1 ratio (E6AP: E6: p53) or 1:3:3:3 ratio (NCP:E6AP:E6:p53) for nucleosome containing samples and incubated at room temperature for 30 min. Data were acquired on a Refeyn OneMP mass photometer. 18 μL of MP buffer was added into the flow chamber followed by focus calibration. 2 μL of protein solution was then added to the chamber and movies of 60 or 90 seconds were acquired. Each sample was measured at least two times independently (n=2) and acquired movies were processed and molecular masses were analyzed using Refeyn Discover 2.3, based on a standard curve created with BSA and thyroglobulin.

Fluorescence polarization

Cy5-labeled DNA containing the canonical p53 motif (5'-Cy5-AGG ACT AAC ATG CCC GGG CAT GTC TAA GCT-3') was used as a fluorescent tracer. Increasing amounts of E6-E6AP with equimolar p53 were mixed with tracer (10 nM final concentration) in a black 384-well microplate (Greiner, 784076) and incubated for 15 min at room temperature. The interaction was measured in a buffer containing 50 mM Tris pH 7.5, 100 mM sodium chloride, and 0.1% (v/v) pluronic acid. Changes in fluorescence polarization were monitored by a PHERAstar FS microplate reader (BMG Labtech) equipped with a fluorescence polarization filter unit. Fluorescence polarization [mP] was plotted versus protein concentration and fitted assuming a one-to-one binding model to determine the dissociation constant (*K*d) using *Prism 9* (GraphPad). Since the oligonucleotide that was used contained a fluorescent label, we refer to these as apparent *K*d (Kd (app)). All measurements were performed in duplicates. For the competitive titration assays, the E6AP-E6-p53 ternary complex bound to the fluorescent oligo tracer was back titrated with unlabeled oligo either containing the p53 motif or with a jumbled sequence. The competitive titration experiments were carried out by mixing tracer (10 nM), E6-E6AP (100 nM) and p53 (100 nM) and increasing concentration of different oligos (0 – 10 mM).

XL-MS

The nucleosome and proteins were mixed in 1:4.5 ratio in MS sample buffer (50 mM HEPES pH 7.5, 150 mM sodium chloride and 500 μM TCEP), and incubated for 30-45 min at room temperature. Crosslinking reagent disuccinimidyl sulfoxide (DSSO) (Thermo Fisher Scientific, A33545) was warmed up to room temperature and diluted to a 100 mM stock concentration in DMSO by shaking at 400 rpm for 5 minutes. The incubated sample was transferred to a concentrator (Amicon Ultra, Merck Millipore, 10,000 MWCO), DSSO was added, and the crosslinking reaction mix was incubated for 1 h at 10 °C, while shaking at 400 rpm. 1 M Tris pH 6.8 (50 mM final concentration) was added to quench the excess crosslinker, while shaking at 400 rpm at room temperature for 1 h. The excess reagent and non-crosslinked proteins were removed by centrifugation at 14,000g for 5 minutes. 400 μL of fresh 8 M urea in 50 mM HEPES, pH 8.0 was added to the concentrator for denaturing and washing, followed by centrifugation at 14,000g for 5 minutes. The step was repeated twice, and the sample was concentrated to a final volume of 50 μL. Next, reduction/alkylation buffer (50 mM TCEP, 100 mM 2-chloroacetamide) was added (5 mM and 10 mM final concentration respectively) and incubated for 90 min at 400 rpm. The concentrator was washed twice (centrifugation at 14,000 rpm, 5 min) with 8 M urea in 50 mM HEPES pH 8.0, and finally washed with 5 M urea in 50 mM HEPES pH 8.0 while concentrating sample to ∼30 μL. Lys-C was added (0.2 μg μL^{-1} stock, 1:75 enzyme to protein ratio) and the sample was digested for 1.5 h at room temperature while shaking. The sample was diluted 2.5-fold with 50 mM HEPES pH 8.0. Trypsin (0.2 mg mL^{-1} stock, 1:50 enzyme to protein ratio) was added and the sample was incubated overnight at 37 °C, while shaking at 400 rpm. An additional aliquot of trypsin (1:100 enzyme to protein ratio) and acetonitrile to a final concentration of 5% was added the next day and the sample was incubated for 5-6 h at 37 °C, while shaking at 400 rpm. The sample was transferred into an Eppendorf tube, TFA was added (1% final concentration), the sample was briefly sonicated and centrifuged for 5 min at 20,000 g. The supernatant was desalted using a PreOmics iST-NHS kit and concentrated in a speedvac. Samples were reconstituted with 0.1% TFA in 2% acetonitrile.

Samples were analyzed by LC–MS in two ways:

1. EASYnLC-Orbitrap Fusion Lumos: Approximately 1 mg of peptides per sample in 0.1% TFA and 2% acetonitrile in water were loaded onto a uPAC C18 trapping column, and then separated on a 50 cm uPAC C18 HPLC column (connected to an EASY-Spray source (all Thermo Fisher Scientific, columns formerly from Pharmafluidics)) connected to an Orbitrap Fusion Lumos. The following chromatography method was used: 0.1% formic acid (buffer A), 0.1% formic acid in acetonitrile (buffer B), flow rate 500 nL/min, 240 min in total, (mobile phase compositions in % B): 0–5 min: 3–7%, 5–195 min: 7–22%, 195–225 min: 22–80%, 225–240 min: 80%.
2. Vanquish Neo- Orbitrap Eclipse with FAIMS: Approximately 2.5 mg of peptides per sample in 0.1% TFA and 2% acetonitrile in water were loaded onto a Vanquish Neo chromatography system with a two-column set-up. Samples were injected onto a trapping column at a constant pressure of 1,000 bar. Peptides were chromatographically separated at a flow rate of 500 nL/min using a 142 min method, (mobile phase compositions in % B): 0-4 min: 2–7%, 4-82 min: 7–20%, 82-112 min: 20-30%, 112-124 min: 30-36%, 124-128 min: 36-45%, 128-142 min at 100% B (buffer A: 0.1% formic acid; buffer B: 0.1 formic acid in 80% acetonitrile) on a 15-cm EASY-Spray Neo C18 HPLC column mounted on an EASY-Spray source connected to an Orbitrap Eclipse mass spectrometer with FAIMS (all Thermo Fisher Scientific).

In either case, the mass spectrometer was operated in MS2_MS3 mode, essentially according to a previous report.[91] Peptide MS1 precursor ions were measured in the Orbitrap at 120 k resolution. On the Orbitrap Eclipse, three experiments were defined in the MS method, with different FAIMS compensation voltages, −50, −60 and −75 V, respectively, to increase the chances of identifying more highly charged peptides (i.e. crosslinked peptides).

Crosslink- and density-guided docking simulations

A python script available under https://github.com/fmi-basel/gthoma_rosetta-density-crosslink-docking was used to run crosslink- and density-guided docking. Detailed flags and parameters for the respective protocols are included in the script. In brief, the model was subjected to ten trials of prepacking and the model with the best total energy score was selected for centroid docking generating

50,000 poses. The poses were then scored with the RosettaDensityScoring protocol and solvent accessible crosslink distances were calculated with Xwalk. In case of homomeric proteins, the shortest distance for each possible chain combination is selected. The density and crosslink scores were normalized by minimum and maximum values and the poses were clustered by RMSD using AgglomerativeClustering from the scipy library. RMSD values were calculated with the pyRMSD library and a distance threshold of 5 A was used for clustering. From each cluster, the pose with the highest average score calculated from the density and crosslink scores (equal weight) was selected. From the selected cluster poses, the top 5 poses were subjected to local docking generating 2,000 poses, respectively. For the resulting poses, the density- and crosslink scores were calculated as before and combined with the interface energy score from rosetta (I_sc). After clustering, the best pose for each cluster was selected based on the average score calculated using a weight of 0.33 for each individual score.

Cryo-EM sample preparation

Nucleosomes were incubated with excess of respective proteins (molar ratio: 1:4.5) in a volume of 60-100 μL at room temperature for 45 minutes in a binding buffer containing 10 mM Tris-HCl pH 7.5, 10 mM potassium chloride, 1 mM magnesium chloride, 10 μM zinc chloride, 1 mM DTT and 5% glycerol. For p53 bound nucleosome complexes, the samples were prepared by using crosslinking reagents as well as without. For the non-cross-linked samples, following incubation, the samples were concentrated to a final volume of ~20 μL. The concentration of the samples was determined by measuring the DNA concentration at an absorbance of 260 nm. For the crosslinked samples, the samples were crosslinked following the GraFix method.[67] For GraFix crosslinking, the nucleosome-protein complexes were added to the top layer of 10-30% (w/v) sucrose gradient (20 mM HEPES pH 8.0, 100 mM potassium chloride, 0.5 mM magnesium chloride, 0.5 mM TCEP) with ~0.2% glutaraldehyde added to the 30% sucrose (w/v) layer. The complex was subjected to ultracentrifugation (Beckman SW60Ti rotor, 37,000 rpm, 14 h, 4 °C). 100 μL fractions were collected and analyzed by native PAGE. The peak fractions were combined, and the sucrose was removed by dialysis into GraFix buffer (20 mM HEPES pH 8.0, 100 mM potassium chloride, 0.5 mM magnesium chloride, 0.5 mM TCEP). The resulting sample was concentrated with an Amicon Ultra 0.5-mL centrifugal filter. After concentration, ~3 μL sample was applied to EM grids. The grids were glow discharged with a Pelco EasyGlow (15 mA current, 45 seconds) prior to application of the sample. Grids were blotted for 3 s at 4°C 90% humidity in a Vitrobot Mark IV (FEI), and then immediately plunged into liquid ethane.

Cryo-EM data collection (see Table 1 Statistics for details)

Except for the p53-NCP$^{SHL+5.9}$ XL dataset that was recorded with a Glacios (Thermo Fisher Scientific) operating at 200 kV, the p53-NCP datasets were collected on a Cs-corrected (CEOS GmbH) Titan Krios (Thermo Fisher Scientific) operating at 300 kV.

The E6AP containing datasets were collected on a Glacios operating at 200 kV.

The Automatic data collection on both microscopes was performed with EPU (Thermo Fisher Scientific).

Cryo-EM image processing

Real-time evaluation was performed using CryoFlare1.10[92] during acquisition. Images were motion-corrected using Relion3 motioncorr implementation[93] by applying a dose-weighting scheme to generate a motion-corrected sum of all frames. CTF estimation was done using the patch CTF implementation in cryoSPARC v.3 or v.4.[94] Particles were picked using either blob picker or template picker in cryoSPARC v.3 or v.4.[94] Each dataset was further processed in cryoSPARC v.3 or v.4[94] which included 2D and 3D classification, 3D refinement and CTF refinement. To improve the quality of the EM density for the p53 DBDs, the particles were imported into Relion and analyzed with multi-body refinement in combination with Blush. Resolution values reported for each reconstruction were calculated based on the gold-standard Fourier shell correlation curve (FSC) at 0.143 criterion,[113] correcting for the effects of soft masks using high-resolution noise substitution.[114] Local resolution for each final map was estimated using local resolution estimation implemented in Relion or MonoRes (XMIPP) implementation in cryoSPARC v.3 or v.4.[115]

Model building and refinement

For modelling of p53 bound to the NCP, PDB:6T93,[9] was used as a template for the nucleosome, and combined with the p53 tetramer coordinates form PDB:3KMD.[74] The models were fitted into the cryo-EM map using ChimeraX[95] and the nucleosomal DNA was extended and its sequence adjusted based on the motif position of the respective structure. The DNA was extended by joining it with B-form DNA generated in Coot[96] and flexible fitting in Isolde[97] with DNA-specific adaptive distance and torsion restraints. This was followed by flexible fitting of the whole model using adaptive distance restraints. Restraints for p53 and its DNA motif were derived from PDB:3KMD,[74] and self-restraints were generated for the rest of the model.

A model for USP7 in complex with p53-bound NCP was obtained by predicting the complex of p53^{TET} and USP7^{TRAF} with Alphafold multimer (v2.3)[98] using PDB:2FOO,[33] as a multimer template (chain masking removed during prediction). The obtained model was merged with the predicted model for full-length USP7 (Alphafold database accession Q93009, model version 4, https://academic.oup.com/nar/advance-article/doi/10.1093/nar/gkad1011/7337620) replacing the USP7^{TRAF} domain with the predicted model for the USP7^{TRAF}-p53^{TET} complex in Coot. This model was combined with the p53^{DBD}-NCP$^{SHL-5.7}$ model followed by rigid-body and flexible fitting. For flexible fitting in ISOLDE, rigid USP7 domains were separately restrained, allowing flexibility between the domains around the linker regions. Inter-chain crosslinks were used as additional single distance restraints.

All models were subjected to a final round of refinement with PHENIX[99] real-space refinement using strong coordinate restraints. This step also included B-factor refinement. Molprobity (v.4.5.2)[100] and PHENIX[99] were used for validation. Side-chains of p53 and USP7 were not resolved in the maps and truncated to Cβ atoms.

The structure of full-length E6AP was first predicted with Alphafold2[98] and docked into the map of the monomeric ternary complex, along with E6 and p53 chains from the previous crystal structure of the ternary complex (PDB: 4XR8)[69] using the ChimeraX fit-in-map.[95] Restrained flexible fitting was done with ISOLDE,[97] and local corrections were done with Coot[96] and ISOLDE. B-factor fitting and coordinate-constrained minimization was done with Phenix real-space refine.[99] The dimeric ternary complex model was built by docking two copies of the monomeric complex model into the dimeric map using ChimeraX fit-in-map, followed by local corrections done in ISOLDE and B-factor fitting using Phenix real-space refine. Validation was carried out with Phenix, Molprobity,[100] and EM-Ringer.[101] Figures were prepared with ChimeraX.

Simulation of p53 nucleosome clash scores

To simulate the clashes of p53 with a nucleosome at all possible DNA motif positions, the DNA of PDB 6T93 was extended at both ends by adding 27 additional base pairs in PyMOL.[102] The DNA trajectory was fitted to the p53-NCP$^{SHL-5.7}$ and p53-NCP$^{SHL+5.9}$ models at both ends using DNA-specific distance and torsion restraints in ISOLDE.

A model of p53 and its DNA motif (sequence) were iteratively moved in +1 steps over the DNA of the NCP model by aligning the phosphate atoms of the p53 DNA motif to the same number of phosphate atoms from +1 shifted segments of the nucleosomal DNA using PyMOL. At each position atom clashes between p53 and NCP were calculated using an atom radius of 1 A. The corresponding script is available under https://github.com/fmi-basel/gthoma_scan-factor.

ChIP-seq

Mouse ES cells (1.5×10^7) were seeded into 15-cm plates the day before the experiment. Where applicable, the media were exchanged with fresh media containing 1 μM doxorubicin (44583, Sigma-Aldrich) in the morning 4 h before harvesting of cells. ChIP with anti-Usp7 (A300-033A, Thermo Fisher Scientific) was carried out as previously described with the following modifications: (1) chromatin was sonicated for 22 cycles of 20 s on and 40 s off using a Diagenode Bioruptor Pico; (2) 75 μg of chromatin was used per immunoprecipitation; (3) protein A magnetic Dynabeads (Thermo Fisher Scientific) were used. Immunoprecipitated DNA was subjected to library preparation (NEBNext Ultra II DNA Library Prep Kit, Illumina). In the library preparation protocol, samples were amplified using 12 PCR cycles. Libraries were sequenced on an Illumina HiSeq (50 cycles) or NextSeq (paired-end, 75 cycles). For control datasets, anti-IgG (M7023, Sigma-Aldrich) was used to control for bead and antibody-unspecific enrichments.

Deubiquitination of ubiquitin chains

The activity of full-length USP7 was tested on labeled tetra-ubiquitin chains: K-48-Fluorescein and K-63-TAMRA (LifeSensors) in presence of nucleosome containing the p53 motif at SHL-5.7. The reaction was carried out in a buffer containing 50 mM HEPES pH 8.0, 50 mM sodium chloride, 5 mM DTT and 1 mM EDTA pH 8.0 for 90 minutes at 37°C. The cleaved product was detected by Typhoon FLA 9500 for the respective labels, and the histone bands were analyzed by SDS/PAGE and Coomassie staining.

Deubiquitination of minimal substrate Ub-rhodamine 110

The enzymatic activity of USP7 was measured using the fluorescence of released rhodamine upon cleavage of the rhodamine-labeled ubiquitin substrate, Ub-rhodamine (Ubiquitin-Rhodamine110Gly, Ub-Rh110Gly-UbiQ-002) (UbiQ). The reactions were performed in running buffer (20 mM HEPES, pH 7.5, 100 mM sodium chloride, 1 mM DTT, 1 mM EDTA and 0.05% v/v Tween-20) on a low binding, clear bottom, 384 well-plates (Greiner) keeping a reaction volume of 20 μL. Top concentration of Ub-rhodamine was 8 μM (final concentration) and was 2-fold diluted till 0.0625 μM. To test the activity of USP7 (1 nM) in complex with the proteins, excess of p53 (4 μM) and nucleosome (100 nM) were used. The nucleosome used in the assay was reconstituted with histone octamer and DNA containing the p53 motif at SHL-5.7. The release of rhodamine was measured at the emission wavelength of 520 nm (±10 nm) after excitation at 485 nm (±10 nm) in a FDSS plate reader.

EMSA

Nucleosomes (30 nM) reconstituted with p53 motif at SHL-5.7, SHL-7.4 and SHL-7.7 nucleosomal sites (NCP$^{SHL-5.7}$, NCP$^{SHL-7.4}$, NCP$^{SHL-7.7}$) were incubated with increasing concentrations of p53 (0-1000 nM). p53 dilutions were prepared in a buffer consisting of 20 mM HEPES pH 8.0, 150 mM NaCl, 0.5 mM TCEP and 5% glycerol. The reactions were conducted in binding buffer (BB) (10 mM Tris-HCl pH 7.5, 10 mM KCl, 1 mM $MgCl_2$, 10 μM $ZnCl_2$, 1 mM DTT, 5% glycerol and 0.5 mg/mL) and incubated at room temperature for around one hour. Following incubation, the samples were analyzed by electrophoresis on a 6% non-denaturing polyacrylamide gel (acrylamide: bis =37.5:1) in 0.5x TGE buffer (12.5 mM Tris base, 96 mM glycine and 500 μM EDTA). The bands were visualized with a Typhoon FLA 9500 after staining in SYBR GOLD Nucleic Acid Gel Stain (Invitrogen). For the binding experiment with p53 and USP7 on nucleosome, nucleosome (30 nM) containing p53 motif at SHL-5.7 (NCP$^{SHL-5.7}$) was incubated with increasing concentrations of USP7 (0- 5000 nM) in presence and absence of p53 (300 nM). The reactions were conducted in BB as described above and the bands were quantified using ImageJ software.

FIDA measurements

Atto488-labeled DNA or nucleosomes was used as a fluorescent tracer. Large scale generation of DNA was performed using Phusion PCR amplification with a Widom 601 sequence template, as noted above, using the following primer pair: 5'-Atto488-ATC CTG GAG AAA CAT GCC CGG GCA TGT CCT CAA TTG GTC GTA-3' and 5'-ATC ACA GGA TGT ATA TAT CTG ACA CGT GC-Atto488-3'. For nucleosome measurements this DNA was used to form NCPs, as described above.

All measurements were performed on a Fida 1 instrument (Fida biosystems, Denmark), using a LPA-coated standard 1 m capillary with a 75 μm diameter (Fida biosystems, Denmark). Samples were injected from the compatible V-bottom 96 well plate provided from the supplier and from the standard 50-vial holder. The green/yellow detector with excitation at 485 nm with LED and emission recorded with long-pass filter of 510 nm was used. Measurements were conducted using the following method sequence with both trays kept at 4°C and the capillary at 10°C:

Tray	Vial	Pressure (mbar)	Time (s)	Outlet	Measure	Comment
2	1	3500	20	1	No	H3PO4
2	2	3500	20	1	No	Buffer rinse + equilibration
1	Analyte	3500	20	1	No	Analyte fill
1	Indicator	50	10	1	No	Inject indicator
1	Analyte	400	240	1	No	Mobilize and measure

Data for each measurement point was processed in the FIDA analysis software (Fida Software V3.0).

QUANTIFICATION AND STATISTICAL ANALYSIS

SeEN-seq analysis

Sequencing reads were mapped to the DNA library pools (either the W601 or 20 bp linker W601) using the Bioconductor package QuasR with default settings,[104] which internally uses bowtie for read mapping.[105] Using the QuasR function Qcount, the number of reads aligned to each construct was quantified, with all library constructs represented. Finally, to calculate SeEN-seq enrichments, the fold change between library-size normalized read counts for each W601-p53 variant in the TF-bound and unbound nucleosome fractions was determined. Three technical replicates were performed for each experimental condition and average enrichment values were plotted using GraphPad Prism 10 software (Figures 1B and S2A).

CUT & RUN analysis

CUT & RUN datasets were aligned to either the mm10 mouse assembly using the QuasR[103,104] Bioconductor package that utilizes Bowtie[105] (RBowtie package). Alignments were performed with the default settings and allowing for uniquely mapping reads. Peak calling on all datasets were performed with MACS2[106] (version 2.1.3.3) using the callpeak argument with default settings and specifying the genome size with -g mm for mouse. Peaks were called using matched GFP-cut and run datasets as controls. Peaks from replicate datasets and across different samples were unified by sorting and merging overlapping regions using the bedtools[116] (version v2.25.0) 'sort' and 'merge' functions with default settings. Read counts over defined genomic regions (i.e., peak regions) were performed using the QuasR[104] function qCount with default parameters and shifting the reads to half of the fragment length. Briefly, counts were normalized between datasets being compared, a pseudo-count of 8 was added and data were log2-transformed. Normalization was performed by multiplying counts by a scaling factor that was determined by the library with the lowest number of mapped reads between the datasets, i.e., scaled down to the smaller library: Scaling factor χ=min(Sample1, Sample2… Sample χ)/Sample χ, where Sample1, Sample2, Sample χ are the total number of mapped reads in each respective sample. The pseudo-count of 8 was used to decrease noise at low read counts between samples. Enrichments of log2 Cut and run readcounts were calculated by subtracting the matched log2 counts from corresponding control datasets. V-plots were generated to visualize nucleosome features of TF-binding sites.[56]To generate v-plots, motifs were first identified by scanning the mouse mm10 genome for the p53 weight matrix derived from the Jaspar MA0106.3 p53 motif using the matchPWM function from the Biostrings R package.[117] Matching sequences were determined by requiring a log2-odds score of at least 10 over a uniform background. In cases where two (or multiple) matches overlapped (ignoring their strands), only the match with the highest log2-odds score was retained. V-plots were generated using all predicted motifs overlapping a p53 ChIP-seq peak. Briefly, read information including position and insert size were extracted using the ScanBamParam function from Rsamtools (Morgan, 2016 #645) with default parameters and with hasUnmappedMate=FALSE and isProperPair=TRUE, for reads withing 1kb either side of predicted motifs. The function bkde2D from the KernSmooth(Wand, 2021 #646) package was used to generate a density matrix of insert size and read lengths, with the arguments gridsize=c(151, 80), range.x=list(c(-500, 500), c(40, 500)) and bandwidth=c(5, 5), and the resulting matrix values were divided by the sum of all values and then multiplied by the number of fragments recorded. Finally, a pseudocount value of 8 and the data were log2 transformed, control dataset signal were subtracted from that of p53 Cut and run and the data were visualized using the image function from the graphics[118] R package. To query motif positions around nucleosome sized fragments, read information including

position and insert size were extracted as above and retaining nucleosome sized fragments (147±51bp). The positions of fragments relative to the centre-point of genomic p53 motifs were generated using the findOverlaps function from the GenomicRanges[119] package and these were averaged across replicate datasets. Data were smoothed for visualization using the stat_smooth function in ggplot2[120] using the arguments method = "lm", formula = y ~ poly(x, 21) and se = FALSE (Figures 1B and S1).

Fluorescence polarization analysis

The fluorescence polarization [mP] *vs.* the nucleosome or DNA concentration were fitted with a nonlinear regression curve to obtain the IC50 values in *Prism 9* (GraphPad). Two technical replicates were measured for each reaction.

XL-MS analysis

MS raw data were analyzed in Proteome Discoverer v.2.5 (Thermo Fisher Scientific) using a Sequest[121] database search for linear peptides, including crosslinker modifications, and an XlinkX[91] search to identify crosslinked peptides. MS2 fragment ion spectra not indicative of the DSSO crosslink delta mass were searched with the Sequest search engine against a custom protein database containing the expected protein components, as well as a database built of contaminants commonly identified during in-house analyses, from MaxQuant[122] and cRAP (ftp://ftp.thegpm.org/fasta/cRAP), using the target-decoy search strategy.[123] The following variable crosslinker modifications were considered: DSSO hydrolyzed/+176.014 Da (K); DSSO Tris/+279.078 Da (K), DSSO alkene fragment/+54.011 Da (K); DSSO sulfenic acid fragment/+103.993 Da (K), as well as oxidation/+15.995 Da (M). Carbamidomethyl/+57.021 Da (C) was set as a static modification. Trypsin was used as the cleavage reagent, allowing a maximum of two missed cleavage sites, peptide lengths between 4 or 6 and 150, 10 ppm precursor mass tolerance and 0.02 Da fragment mass tolerance. PSM validation was performed using the Percolator node in PD and a target FDR of 1%.

XlinkX v.2.0 was used to perform a database search against a custom protein database containing the expected complex components to identify DSSO-crosslinked peptides and the following variable modification: DSSO hydrolyzed/+176.014 Da (K); oxidation/+15.995 Da (M). Crosslink-to-spectrum matches (CSMs) were accepted above an XlinkX score of 40. Crosslinks were grouped by sequences and link positions and exported to xiNET[124] format to generate crosslink network maps.

Crosslinks were mapped to the structure models with an in-house script for PyMOL and the ChimeraX plug-in XMAS.[125] Xwalk was used to calculate solvent accessible surface distances.[126]

Data are available through ProteomeXchange[127] with the identifiers PXD054140 and PXD054141.

ChIP-seq analysis

ChIP-seq datasets were aligned to the mm10 mouse assembly using the QuasR[104] Bioconductor package that utilizes Bowtie[128] (RBowtie package). Alignments were performed with the default settings and allowing for uniquely mapping reads. Peak calling on all datasets were performed with MACS2[106] (version 2.1.3.3) using the callpeak argument with default settings and specifying the genome size with -g mm for mouse. Read counts were generated over defined genomic regions (i.e. peak regions) using the QuasR[104] function qCount after removing blacklisted regions,[129] with default parameters and shifting the reads 80 bp, which was approximately half the size of ChIP-seq library fragments. Briefly, counts were normalized between datasets being compared, a pseudo-count of 8 was added and data were log2-transformed. Normalization was performed by multiplying counts by a scaling factor that was determined by the library with the lowest number of mapped reads between the datasets, i.e., scaled down to the smaller library: Scaling factor χ= min(Sample1, Sample2… Sample χ)/Sample χ, where Sample1, Sample2, Sample χ are the total number of mapped reads in each respective sample. The pseudo-count of 8 was used to decrease noise at low read counts between samples. Enrichments of log2 ChIP-seq readcounts were calculated by subtracting the matched log2 counts from corresponding control datasets. Similarly, changes in binding were calculated by the difference in log2 ChIP-seq readcounts between datasets. To define a reference set of USP7 peaks from the replicate experiments with or without p53 activation, the consensus peak calling was carried out as follows: MACS2 peaks from individual replicates were assembled using R package DiffBind[130,131] (v3.2.4) to generate a non-overlapping set of genomic peaks. As described in the Encode project,[132] Irreproducibility Discovery Rate (IDR) analysis[133] was applied to define a reliable set of consensus peaks using a threshold of IDR <0.01, average ChIP-seq enrichment >2 and a minimum ChIP-seq enrichment of 0.5 in each replicate. Heatmaps were generated by counting the 5' positions of mapped reads relative to defined genomic regions (i.e. peak regions) using the QuasR[104] function qProfile and visualized using the EnrichedHeatmap[107] Bioconductor package (version 1.26.0). In brief, qProfile was run with default parameters, for 1kb regions centered on the middle of peak regions and shifting the reads 80bp, which was approximately half the size of ChIP-seq library fragments, or to the fragment midpoint for paired-end libraries. Resulting counts/peak region were scaled by 1e6/total reads in each sample and multiplied by 1e3, then smoothed by calculating a running mean of 20bp across the normalized counts. These were converted into normalized matrixes, replicates averaged, and visualized using the as.normalizedMatrix and EnrichedHeatmap functions from the EnrichedHeatmap[107] R package. Color scales were implemented manually based on enrichment values and using the colorRamp2 function within the Circlize[134] R package. Publicly available p53 ChIP-seq and IgG control datasets were utilized in this study to contrast binding (GEO accession identifiers GSM6038035, GSM6038036, GSM6038037, GSM6038038, GSM6038043 and GSM6038044). Similarly, publicly available DNase1 Sequencing datasets from mouse stem cells (GEO accession identifiers SRR1973528, SRR1973529) were utilized in this study to contrast with Usp7 binding, where Log2 read counts were generated over Usp7 binding sites as described above for ChIP-seq datasets.

Deubiquitination of minimal substrate Ub-rhodamine 110 - analysis

The data was analyzed for obtaining the kinetic parameters using Prism 10 (GraphPad). Two technical replicates were measured for each experiment.

EMSA quantification

The EMSA experiments were performed in duplicates and the bands were quantified using ImageJ software. For p53-nucleosome binding experiments (Figures S2B–S2E), the curve (plotted mean with SD) appeared sigmoidal, and hence to facilitate quantification, the K_d was approximated by calculating the half maximal binding. For estimating the fraction bound of USP7 (Figures S15 A and S15B), the raw signal of nucleosome-bound p53 was subtracted from each tested concentration of USP7 and the resultant signal was plotted against the total signal. The binding curve was fit using one site specific binding model on GraphPad Prism 10 software for estimating an approximate K_d. Three way bar plot (plotted mean with SD) (Figure S15C) was plotted using GraphPad Prism 10 software to illustrate USP7 binding on nucleosome-bound p53 (bar shown in blue), and to have a comparative analysis with total protein binding on nucleosome (bar shown in pink) and reduction of unbound nucleosome upon protein binding (bar shown in yellow).